The International Journal of Advanced Manufacturing Technology
https://doi.org/10.1007/s00170-023-12764-5

ORIGINAL ARTICLE

Optimization of laser-cladded SS316L/IN625 functionally graded material deposited on a copper substrate for boiler pipe heat exchanger applications

Joseph B. Morake[1] · Martin R. Maina[1] · James M. Mutua[1] · Eyitayo O. Olakanmi[2,3,4] · Sisa L. Pityana[5]

Received: 11 August 2023 / Accepted: 22 November 2023

Abstract
Laser cladding is a surface modification method that can be employed in components under severe operating conditions, such as boiler heat exchangers, to mitigate degradation. However, poor clad quality hinders performance during service. This study employed the hybrid Taguchi-grey relational analysis and artificial neural network (ANN) method to optimize the clad qualities while varying the laser cladding process parameters including laser power, scanning speed, and powder flow rate. Laser cladding process parameters were used in the backpropagation NN model as input, and the grey relational grade was employed as the output of the model to improve the clad properties. The values of performance attributes for microhardness and aspect ratio were increased, whereas surface roughness and porosity were reduced in the fabricated functionally graded stainless steel 316L/Inconel 625 coating. When the ANN model was used to optimize the experimental grey relational analysis conditions, it was found that the 600 W laser power, 700 mm/min scanning speed, and 1.5 g/min powder flow rate enhanced the experimental output. The generated model significantly improved the quality of the laser cladding process. A confirmatory experiment was carried out using ANN optimal parameters, and the fabricated samples were subjected to microscopic analysis to ascertain the influence of process parameters on clad characteristics. Heat treatment was also used to alleviate the tensile residual stresses of the fabricated functionally graded material. Thus, the ANN model and fabricated coating can be utilized effectively to modify the boiler pipe surface.

Keywords Artificial neural network · Grey relational analysis · Laser cladding · Optimization · Multi-performance characteristics

1 Introduction

Boiler pipes frequently experience wear and corrosion-related problems in severe operating conditions, leading to power plant interruptions and high maintenance costs. The degradation is usually aggravated by manufacturing defects such as pores and cracks, which allow for the penetration of oxides and crack propagation through poor microstructural interface [4, 10]. Kuznicka et al. [13] reported on the erosion-corrosion of copper heat exchanger pipes and attributed its cause to tube perforations resulting from excessive fluid pressure containing chloride ions, which eroded the protective cuprous oxide layer. Cozzarini et al. [8] investigated heat exchanger copper pipe failure and concluded many tiny cracks originating from the outside surface of the boiler that had penetrated the tube through the copper grain boundary. This shows that improving the surface characteristics of

✉ Joseph B. Morake
josephblmorake@gmail.com

1 School of Mechanical Manufacturing and Materials Engineering, Jomo Kenyatta University of Agriculture and Technology (JKUAT), Nairobi, Kenya

2 Department of Mechanical, Energy & Industrial Engineering, Botswana International University of Science & Technology, Palapye, Botswana

3 UNESCO Chair On Sustainable Manufacturing & Innovation Technologies (UCoSMIT), Botswana International University of Science & Technology, Palapye, Botswana

4 Advanced Manufacturing & Engineering Education (AMEE) Research Group, Botswana International University of Science & Technology, Palapye, Botswana

5 Laser Enabled Manufacturing Research Group, Council for Scientific & Industrial Research, Pretoria, South Africa

boiler pipe materials is necessary, as it protects the copper pipes from degrading attacks.

To reduce the frequency of these failures, single alloy coatings such as stainless steels 316L (SS316L) and Inconel 625 (IN625) are often used as surface modifiers. SS316L is frequently utilized because of its superior intergranular corrosion resistance at high temperatures, which is increased by its higher chromium and molybdenum content, and temperature tolerance up to 850 °C according to Ndumia et al. [19]. Meanwhile, it can become prone to corrosion and wear attack due to low hardness, leading to wear-related failures in aggressive environments. IN625 has high fatigue strength, pitting and crevice corrosion resilience, and excellent formability. However, with longer exposures, it occasionally experiences intergranular corrosion induced by sulfur and applied stresses. For instance, stress corrosion cracking was determined to be the cause of the failure of SS304L heat exchanger tubes when exposed to chloride content at elevated temperatures by Soltani et al. [27]. This demonstrates that tube materials can degrade with time due to inadequacy to meet all required material properties in harsh environments, thus, calling for the use of functionally graded materials (FGMs) for surface modification.

FGMs are a new class of hybrid materials realized through powder compositional grading that is varied spatially through the volume to fulfil a specific purpose at a particular part location according to Owoputi et al. [21]. In this study, an FGM comprising SS316L and IN625 was developed to safeguard boiler copper pipes, a soft material that is often vulnerable to tube wear, hydrogen embrittlement, and stress corrosion cracking on the surface [6, 35]. According to Zhang et al. [34], copper-stainless steel is desirable for heat exchanger applications, but joining copper and SS316L is difficult because the two materials possess distinct characteristics with inherently differing thermomechanical properties, which can result in defect formation like pores and cracks. They indicated that because of the high reflectivity of copper, there is limited solubility at the interface characterized by Cu- and Fe-rich islands that hinder performance. This might be explained by secondary phase formation at the FGM gradient zone, which can result in crack-stress fields and propagation under high-pressure loading during service according to Carroll et al. [5]. However, the authors asserted that several strategies, including process parameter optimization and gradient layers, can be employed to create an excellent metallurgical bond free of defects. Heat exchanger pipe coatings are usually applied at a coating thickness ranging from 50 microns to a few millimiters, depending on the operating conditions such as pressure, pipe thickness, and degradation attacks. Hence, the clad aspect ratio (AR) should be optimized because a bulky clad coating thickness reduces the heat transfer [36].

Liang et al. [14] fabricated a seven-layered FGM comprising SS316L/IN718 via a directed energy deposition (DED) process, and obtained a good interfacial bond characterized by columnar to equiaxed microstructural transformation. Zhang et al. [33] developed a functionally graded SS316L/IN625 on a stainless steel 304L substrate using the DED technique. Results showed a good metallurgical bond at the interface with a sharp structure transition exhibiting gradual change from cellular structure to columnar structure. A thin-walled SS316L/IN625 was built by Mehrabi et al. [18], whose work examined the effects of laser power on the size, weight, height, and microhardness of FGM fabricated by the LMD process. Based on the results, increasing laser power decreased the surface smoothness of the gradient wall and generated variations in microhardness values because of the rapid cooling rates and low-temperature gradients. They identified pore defects in the graded microstructure and as a result, recommended future research focusing on optimizing other process parameters, such as scanning speed, powder size, focal point position, and dwell duration, to minimize microstructural and mechanical defects. This shows that research on the optimization of several process parameters of SS316L/IN625 is scarce in literature but can enhance microstructural properties. Additionally, the cited literature [14, 18, 32] makes it apparent that copper pipes are one of the most widely used materials for boilers, but the fabrication of SS316L/IN625 FGM on pure copper substrates has not been adequately explored. Furthermore, the hybrid optimization of this material combination has not been explored. Based on these findings, the present study deposited SS316L/IN625 FGM on copper substrates using the laser cladding (LC) technique with optimum process parameters.

LC is a well-known additive manufacturing technique used to modify the surface of engineering components operating in hostile environments, such as boiler pipes [3]. A laser-material interaction occurs during the deposition that is characterized by rapid solidification mechanisms, resulting in microstructural transformation or processing defects depending on the nature of the melt pool formed. The melt pool solidification behavior is usually governed by the most influential process parameters, such as laser power, scanning speed, and powder flow rate, according to Elijah et al. [9]. For instance, a larger energy input may lead to adequate particle melting, which raises the microhardness and enhances the wear resistance properties [1, 9]. According to Fatoba et al. [11], AR is the ratio of clad width to clad height and it has a linear relationship with scanning speed because clad height is mainly influenced by scan speed rather than clad width. This could be attributed to higher scanning speed causing less laser beam and powder interaction time during laser deposition, resulting in a bulky layered structure. Riveiro et al. [23] concluded that a less bulky structure is observed in the case of powder flow rate due to the

weight-to-volume ratio. Therefore, it can be argued that a higher AR is required for boiler pipes because it reduces the overall coating costs, increases the heat transfer surface area by decreasing thickness, and reduces microstructural voids and inter-track porosity in bulky FGM clad, which serve as an incubator for corrosive oxides according to Tiwari et al. [28]. Therefore, it is clear that using optimum parameters and comprehending how they affect the clad properties is advantageous for better component performance.

Several statistical and machine learning optimization techniques have been employed to determine optimum DED process parameters. Some well-known techniques include the Taguchi method (TM), grey relational analysis (GRA), and artificial neural network (ANN). The TM is a statistical method used for the design of experiments (DoE) to find optimum experimental conditions by identifying desirable control factors that yield optimum results. Taguchi employs a series of fractional factorial designs based on design matrix based on number of factors, levels of experiments, and degree of parameter interaction. For instance, with L_9 (3^4), nine experiments should be carried out to study the effects of four varying process parameters conducted or repeated at three levels. The TM, however, is limited in optimizing performance characteristics according to Lin et al. [15]. For this reason, it is usually incorporated with the GRA method because it can optimize multi-performance clad quality characteristics according to Simeon et al. [26]. For instance, Yang et al. [31] optimized the input parameters for the scanning speed, powder flow rate, laser power, and overlap ratio on the surface roughness and width error of IN625 LCs using the Taguchi and GRA techniques. The optimum parameters they used to achieve an excellent metallurgical bond also revealed that the overlap ratio was the most influential parameter. Chang et al. [7] utilized the Taguchi-GRA to optimize multiple DED process parameters, which included the overlap ratio, cladding efficiency, laser defocus distance, and laser power, hence, improving the cladding efficiency, porosity, and surface roughness characteristics. The results showed that laser power greatly influences porosity, but powder flow rate, scanning speed, and overlap ratio have a greater impact on surface roughness. Taguchi-GRA procedure, on the other hand, also has some limitations because it necessitates prior knowledge of the correlation between input and output data. The utilization of non-linear models for multi-performance characteristic prediction and optimization, however, makes artificial intelligence techniques, such as ANN, more advantageous. Meanwhile, studies that used Taguchi-GRA and ANN for optimizing DED process parameters are scarce in the literature. Nonetheless, some research has been done in the manufacturing domain for the hybrid optimization of input parameters [22].

Maodzeka et al. [17] employed hybrid optimization combining ANN and response surface methodology (RSM). The authors used the developed model to predict quality characteristics (microhardness, porosity, phase composition, and wear resistance) using process parameters (hatch spacing, scan speed, and laser power) as input data. Results showed a better prediction accuracy of ANN than RSM and the predicted values were consistent with the conducted experiment. This shows that ANN can be used to predict and optimize output characteristics of laser deposited samples and give accurate results. Lin et al. [15] successfully optimized the multi-performance input parameters of gas metal arc welding, including the weld bead width, penetration depth, and fusion area. It was accomplished by combining the L_{16} orthogonal array (OA) of the TM with GRA to obtain the grey relational grade (GRG) for maximizing multi-performance characteristics and to build a neural network database. The Levenberg–Marquardt back propagation (LMBP) algorithm was successfully used to construct an ANN model that can provide a combination of optimal parameters, which showed a 13.91% improvement over the GRA technique.

Koklu et al. [12] studied the effects of feed rate, material direction, and spindle speed machining parameters on the surface finish, delamination, and tool wear. They reported that feed rate is the most influential parameter with a linear relation with delamination and thrust force. To optimize the spark erosion process parameters during electric discharge machining of the hastelloy C-276 [16] combined hybrid GRA and ANN, they observed that the ANN-GRA technique has greater accuracy for predicting performance characteristics and lowering uncertainty after feeding GRA values as inputs to the ANN model. Wakchaure et al. [30] used hybrid grey TM and ANN for the multi-response optimization of the friction stir welding process. The Taguchi L_{27} OA was used to develop input data of process parameters (tool rotation, angle, and welding speed), and the GRG of impact and tensile strength was used as output for prediction and optimization. This demonstrates that ANN can be utilized to improve the optimal parameters obtained using the GRA technique and provides a superior optimization accuracy when compared to GRA applied alone.

In this study, the hybrid optimization of multi-performance clad quality characteristics of functionally graded SS316L/IN625 deposited on a copper substrate was employed using the Taguchi-GRA-ANN approach. The study investigates the effects of LC process parameters, laser power, scanning speed, and powder flow rate on microhardness, AR, surface roughness, and porosity, as well as identifying the optimum LC process parameters that yield appropriate quality characteristics for enhanced performance of boiler copper pipe surface.

2 Materials and methods

2.1 Materials

The FGM was developed from powdered SS316L (+45–90 µm) and IN625 (+45–90 µm), deposited on grade 1(A) pure copper substrate measuring 100 × 50 × 10 mm^3. The materials were supplied by Avimetal AM Tech (PTY) Ltd., South Africa. Figure 1 shows the powder particle shapes, which exhibit a nearly spherical morphology with satellites. This spherical powder morphology can significantly enhance the surface finish and powder deposition efficiency due to its regular surface. The powder chemical composition was verified and is presented in Table 1.

2.2 LC process

Figure 2 shows the LC machine at the Council of Scientific and Industrial Research, Pretoria in South Africa. It consists of a 5 kW IPG YLS fiber laser system with a Kuka robot connected to a two-feeder hopper system, which injects powders through a coaxial nozzle with an argon carrier gas and shielding gas to prevent material oxidation. The argon gas and shielding gas were kept constant during deposition at 18 l/min and 8 l/min, respectively. The laser beam had a 2 mm spot diameter and the standoff distance was kept constant at a 10 mm distance above the substrate with a 60° tilt angle to overcome the high reflectivity of copper during deposition. The first layers were deposited using 1800 W, 600 mm/min, and 2 g/min, to obtain a good metallurgical bond. Initial parameters were established using laser powers of 2700 W, 2400 W, 2100 W, and 1800 W since research on the study to laser clad functionally graded SS316L/IN625 on pure copper substrate is scarce. Apart from the 1800 W parameter, all laser powers between 2100 and 2700 W caused delamination, hence this value was chosen as the appropriate parameter. Higher laser energy input was first employed due to the high reflectivity of copper, which demands a higher energy input to achieve a metallurgical bond between copper and SS316L. The rest of the layers were fabricated based on the Taguchi methodology.

The Taguchi L_9 (3^3) OA was utilized in the DoE before continuous deposition. The LC experiments were repeated three times and labeled TR1, TR2, and TR3 for each of the nine levels. The laser power, scanning speed, and powder flow rate varied from 700–1000 W, 400–600 mm/min, and 2–6 g/min, respectively. Table 2 gives a detailed summary of the matrix. A linear flowability graph with values in revolutions per minute was obtained by measuring the powder flow rate for 2 min and taking an average of three similar experiments. Additionally, a laser track overlap of 50% was used with laser-clad layer thickness kept constant at 0.8 mm. The FGM was built into a five-layer structure with linear compositional variation starting with 100% SS316L to 100% IN625, as shown in Fig. 3.

2.3 Sample preparation and characterization

The fabricated samples were sectioned along the transverse section using the Struers Labotom-15 cutting machine (Struers, France) for mounting, grounding, polishing, microstructural characterization, and mechanical testing. The cross-sectioned part was hot mounted in epoxy resin and ground using abrasive sheets of 120, 320, 800, 1200, and 4000 grit. Polishing was carried out using 9, 6, 3 microns, and active oxide polishing suspension. The samples were then

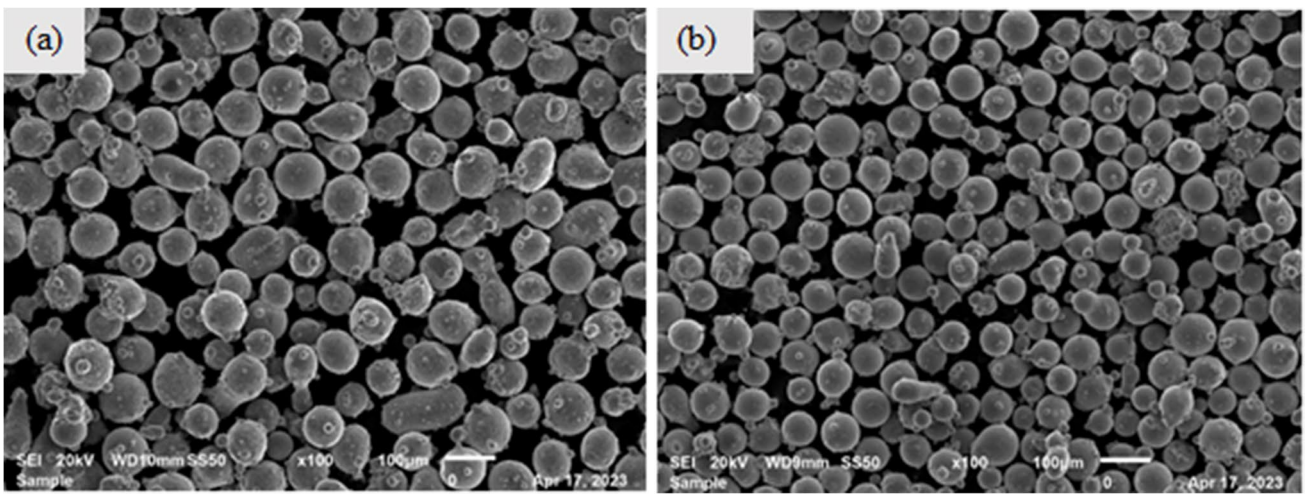

Fig. 1 SEM powder morphology of **a** stainless steel 316L and **b** Inconel 625

Table 1 Chemical composition of SS316L, IN625, and Cu materials (wt.%)

Materials	Fe	Cr	Ni	Cu	Nb	Mn	Si	P	S	C	Al	Ti	Mo
SS316L	Bal.	17.17	10.57	- -	-	1.05	0.64	0.005	0.003	0.01	-	-	2.52
IN625	1.96	21.80	Bal	-	4.10	0.01	0.04	0.01	0.003	0.078	0.22	0.17	9.76
Cu	-	-	-	100.0	-	-	-	-	-	-	-	-	-

electrochemically etched for 5 s using a 50/50 mixture of oxalic acid and water.

The optical microscope (Olympus BX51M, Japan) was used to measure the clad geometry. The clad height and weight were measured to compute the AR (W/H), as illustrated in Fig. 4. The porosity level of the FGM samples was also measured and quantified using optical microscopy images equipped with ImageJ software. This was accomplished by converting them to binary black and white for automatic computations based on contrast level. The microstructure and elemental composition were analyzed using a scanning electron microscope equipped with an energy-dispersive spectrometer (SEM–EDS). A Struers Vickers microhardness tester (Leitz, Germany) was used to measure the microhardness under a force of 10 N for 10.0 s. Adjacent indentations of 1000 µm spacing along the *Y*-axis, which is the FGM buildup direction, 430 µm spacing along the *X* direction, with 0.5 mm spacing across the first clad-substrate build direction were created. Each sample had a total of 13 indentations, and the average was determined using the three samples fabricated for each parameter (Table 2).

2.4 Analysis of data

The Minitab statistical software (21.1.0) was utilized in the Taguchi L_9 OA for the DoE and Taguchi-based GRA analysis. Further, the R2023a MATLAB software was used for the ANN optimization using the LMBP algorithm. This was achieved by using the process parameters as inputs and GRG as the model's output. After optimization, a confirmatory test was carried out using one factor at a time, and the samples were fabricated using LC employing the ANN optimum parameters. The ANN optimum samples were characterized using microstructural analysis to corroborate the effects of process parameters on clad quality characteristics. The micro 360 residual stress analyzing machine (Pulstec, Tokyo) was used to measure residual stresses for optimum sample using a Cu X-ray tube at 45 °C inclination angle and 30 s irradiation time. This was done to confirm if the optimum sample has tensile residual stresses. According to Bhargava and Banerjee [39], the heat treatment of pure copper through annealing process is usually carried out in the temperature range between 375 and 650 °C, and the time at temperature must be controlled between 0.5 and 2 h to control grain growth and oxidation. However, research on the heat treatment of SS316L/IN625 FGM on pure copper is still scarce. Meanwhile, the heat treatment of SS316L/IN625 FGM on mild steel substrate was performed by Rodrigues et al. at 1050 °C for 2 h. Hence, their parameters were adopted for heat treatment conditions in this study to explore the possibility of reducing tensile residual stresses.

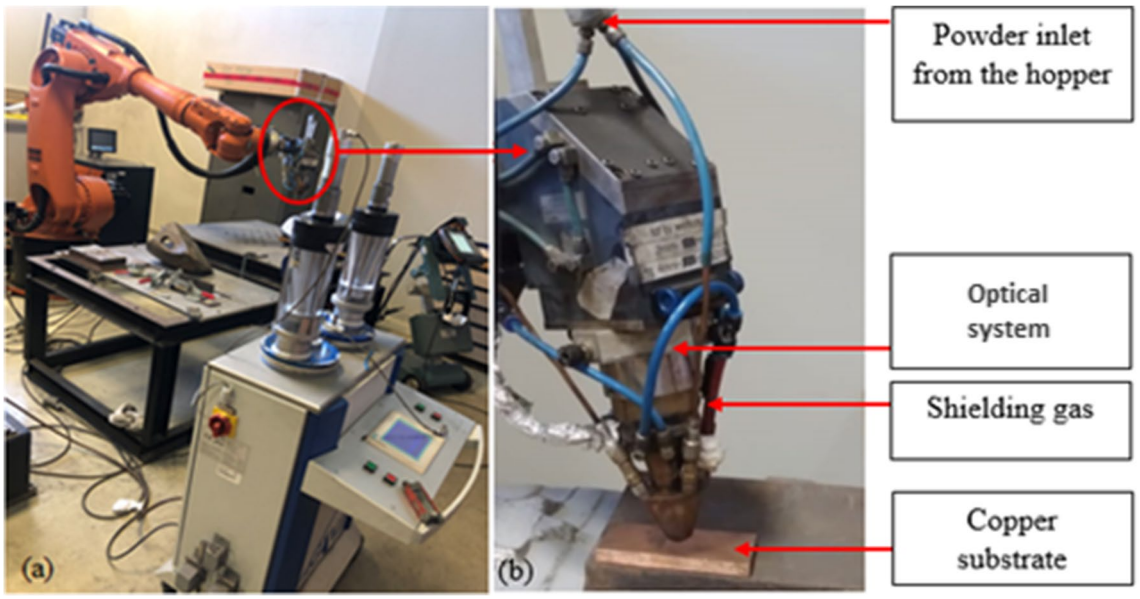

Fig. 2 Laser cladding system **a** Kuka robot with a 5 kW IPG YLS fiber laser system and **b** coaxial nozzle

Table 2 Taguchi L_9 orthogonal array for fabricating SS316L/IN625 FGM

Run	Laser power, W	Scanning speed, mm/min	Powder feed rate, g/min
1	700	400	2
2	700	500	4
3	700	600	6
4	850	400	4
5	850	500	6
6	850	600	2
7	1000	400	6
8	1000	500	2
9	1000	600	4

3 Results and discussion

3.1 Taguchi-GRA

The multi-objective optimization problem was addressed using the GRA method, which used the Taguchi experimental matrix to determine the ideal values. Optimum parameters were evaluated using a five-step procedure: (i) acquiring output responses, (ii) normalization of the data, (iii) computing deviation sequence, (iv) calculating the grey relational coefficient (GRC) and GRG of normalized data, and (v) computing the average GRG using values of the Taguchi matrix.

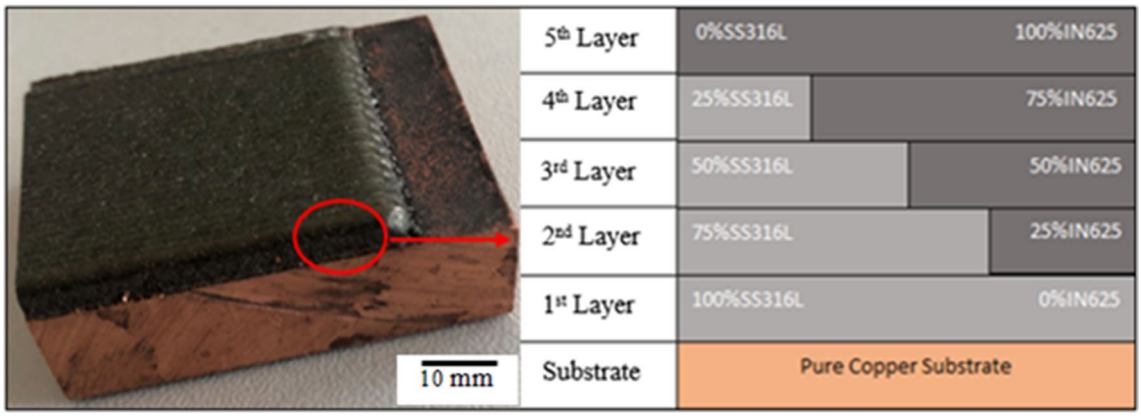

Fig. 3 FGM layer buildup **a** as-built SS316L/IN625 clad and **b** compositional variation (wt.%)

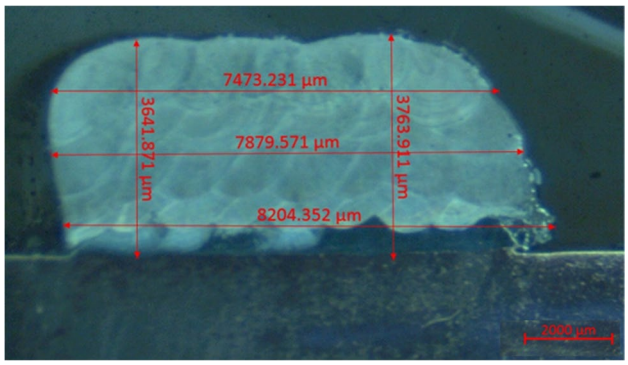

Fig. 4 Cross-sectional measurements of the laser-clad aspect ratio

3.1.1 *Taguchi L_9 OA output data*

The TM uses the relation between the input and the output to determine variance and response settings. The experimental samples obtained from Table 2 of the Taguchi L_9 OA were measured for the quality characteristics (AR, microhardness, and porosity) and the results are shown in Table 3. Thereafter, the results were transformed into Table 4 using signal-to-noise (S/N) ratios of the analysis of variance (ANOVA) method.

3.1.2 Data normalization

The TM reduces variability in a process by minimizing uncontrollable factors called noise factors. Higher S/N values are used to minimize noise factors. Different S/N ratios can be selected to maximize or minimize the responses. In this study, the S/N ratio for higher the better maximized the microhardness and AR, while the S/N ratio for lower the better minimized the porosity and surface roughness. Equations 1 and 2 [16] were used for normalizing larger-the-better and smaller-the-better, respectively. This process is known as data normalization. Based on the S/N ratios, the quality characteristics were normalized from 0 to 1. Table 4 presents the normalized values of the S/N response variables.

Table 3 GRA experimental output responses for quality characteristics

Input parameter				Output parameters											
Aspect ratio (mm)							Microhardness (HV)			Surface roughness (Ra)			Porosity (%)		
Exp	A	B	C	TR1	TR2	TR3	TR1	TR2	TR3	TR1	TR2	TR3	TR1	TR2	TR3
1	1	1	1	1.94	1.95	1.93	235.00	234.00	232.90	6.55	7.11	6.60	0.04	0.04	0.03
2	1	2	2	1.96	1.96	2.03	239.83	238.21	237.65	6.00	6.97	6.10	0.27	0.25	0.34
3	1	3	3	2.12	2.14	2.11	253.00	250.00	245.00	10.75	9.65	10.88	0.18	0.19	0.22
4	2	1	2	1.71	1.70	1.69	221.41	222.40	220.00	11.51	10.10	11.74	0.04	0.03	0.04
5	2	2	3	2.11	1.88	1.90	225.81	227.00	227.30	10.13	11.40	10.10	0.15	0.15	0.17
6	2	3	1	3.59	3.68	3.61	240.67	241.89	242.60	5.66	5.99	5.60	0.03	0.02	0.03
7	3	1	3	1.17	1.15	1.71	207.00	209.00	198.76	14.13	16.80	15.20	0.48	0.57	0.50
8	3	2	2	1.99	2.01	1.92	230.67	233.27	233.40	7.22	8.37	7.50	0.04	0.05	0.04
9	3	3	1	1.43	2.15	2.10	230.34	230.10	230.70	10.73	11.50	10.80	0.34	0.35	0.41

Table 4 Normalized response values for output variables

	Aspect ratio (mm)			Microhardness (HV)			Surface roughness (Ra)			Porosity (%)		
N	TR1	TR2	TR3	TR1	TR2	TR3	TR1	TR2	TR3	TR1	TR2	TR3
1	0.3123	0.3162	0.3083	0.6681	0.6497	0.6294	0.9152	0.8652	0.9107	0.9636	0.9636	0.9818
2	0.3202	0.3202	0.3478	0.7572	0.7273	0.7170	0.9643	0.8777	0.9554	0.5455	0.5818	0.4182
3	0.3834	0.3913	0.3794	1.0000	0.9447	0.8525	0.5402	0.6384	0.5286	0.7091	0.6909	0.6364
4	0.2213	0.2174	0.2134	0.4176	0.4358	0.3916	0.4723	0.5982	0.4518	0.9636	0.9818	0.9636
5	0.3794	0.2885	0.2964	0.4987	0.5206	0.5262	0.5955	0.4821	0.5982	0.7636	0.7636	0.7273
6	0.9644	1.0000	0.9723	0.7727	0.7952	0.8083	0.9946	0.9652	1.0000	0.9818	1.0000	0.9818
7	0.0079	0.0000	0.2213	0.1519	0.1888	0.0000	0.2384	0.0000	0.1429	0.1636	0.0000	0.1273
8	0.3320	0.3399	0.3043	0.5883	0.6362	0.6386	0.8554	0.7527	0.8304	0.9636	0.9455	0.9636
9	0.1107	0.3953	0.3755	0.5822	0.5778	0.5889	0.5420	0.4732	0.5357	0.4182	0.4000	0.2909

$$X_p(j) = \frac{Y_p(j) - \min(Y_p(j))}{\max(Y_p(j)) - \min(Y_p(j))} \quad (1)$$

$$X_p\prime(j) = \frac{Y_p(j) - \min(Y_p(j))}{(\max(Y_p(j)) - \min(Y_p(j))} \quad (2)$$

where $X_p(j)$ and $X_p\prime(j)$ are the normalized S/N ratios, $Y_p(j)$ is the corresponding experimental S/N value, and $\max(Y_p(j)$ and $\min(Y_p(j)$ are the maximum and minimum Taguchi S/N ratio values.

3.1.3 Deviation sequence

The deviation sequence is denoted by $\Delta_{oi}(j)$ and computed using Eq. 3 of the reference sequence $x_o\prime(j)$ and the compatibility sequence $x_i\prime(j)$ to evaluate the complete variance. Table 5 displays the results for the normalized response deviation.

$$\Delta_{oi}(j) = |x_o\prime(j) - x_i\prime(j)| \quad (3)$$

3.1.4 GRC and GRG

The GRC, denoted by δ, measures the correlation between two responses. It is computed using Eq. 4 by Vikram et al. [29]. Thereafter, the GRG is computed by taking the average of all the GRC (MH, AR, SR, P), and the results are presented in Table 6.

$$\delta_{ij} = \frac{\Delta_{min} + \varepsilon\Delta_{max}}{\Delta_{ij} + \varepsilon\Delta_{max}} \quad (4)$$

where ε is the distinguishing coefficient taken as 0.5, Δ is the deviation, and Δ_{max} and Δ_{min} denote the maximum and minimum absolute differences, respectively. Table 6 gives a summary of the GRC and GRG values. The rank was calculated using the GRG values, with the highest values indicating the most desirable clad quality characteristics with favorable conditions.

Table 7 shows the ANOVA response table of the GRG to identify the parameter that most significantly influences the performance attributes. The parameters were ranked by significance using the sum of squared deviation for the entire variability of the GRG. The findings show that, with the highest percentage of 47.36%, scanning speed has the most significant influence on performance characteristics, while laser power and powder flow rate were the least significant with a percentage of 26.33 and 26.31%, respectively. Additionally, the ideal values for the laser power, scanning speed, and powder flow rate correspond to levels 2, 3, and 1 (2–3-1). This implies that the sample six parameters exhibited the highest performance characteristics, including higher microhardness and AR, reduced porosity, and smoother surface, at a laser power of 850 W, scanning speed of 600 mm/min, and powder flow rate of 2 g/min.

Figure 5a shows the interaction of laser power and scanning speed with GRG output of FGM clad quality characteristics (MH, AR, P, and SR). It can be seen that when powder flow rate is set at zero level, the highest GRA output is obtained when laser power and scanning speed are set at 700 to 850 W and 500 to 600 mm/min, respectively. Meanwhile, when scanning speed is set at zero, the GRG output in Fig. 5b shows laser power and powder flow rate interaction, whereby a higher GRG value is obtained at 900 W laser power and 3 g/min of powder flow rate. Figure 5c shows that increasing scanning speed to 6 mm/min and lowering powder flow rate to 2 g/min significantly enhance the clad qualities.

3.2 Optimization using ANN

The topology of the neural network model comprising GRC values as inputs (laser power, scanning speed, and powder flow rate), four hidden layers, and GRG values as the outputs parameter is presented in Fig. 6. The model was created

Table 5 Deviation sequences of the normalized responses

	Aspect ratio (mm)			Microhardness (HV)			Surface roughness (Ra)			Porosity (%)		
N	TR1	TR2	TR3	TR1	TR2	TR3	TR1	TR2	TR3	TR1	TR2	TR3
1	0.6877	0.6838	0.6917	0.3319	0.3503	0.3706	0.0848	0.1348	0.0893	0.0364	0.0364	0.0182
2	0.6798	0.6798	0.6522	0.2428	0.2727	0.2830	0.0357	0.1223	0.0446	0.4545	0.4182	0.5818
3	0.6166	0.6087	0.6206	0.0000	0.0553	0.1475	0.4598	0.3616	0.4714	0.2909	0.3091	0.3636
4	0.7787	0.7826	0.7866	0.5824	0.5642	0.6084	0.5277	0.4018	0.5482	0.0364	0.0182	0.0364
5	0.6206	0.7115	0.7036	0.5013	0.4794	0.4738	0.4045	0.5179	0.4018	0.2364	0.2364	0.2727
6	0.0356	0.0000	0.0277	0.2273	0.2048	0.1917	0.0054	0.0348	0.0000	0.0182	0.0000	0.0182
7	0.9921	1.0000	0.7787	0.8481	0.8112	1.0000	0.7616	1.0000	0.8571	0.8364	1.0000	0.8727
8	0.6680	0.6601	0.6957	0.4117	0.3638	0.3614	0.1446	0.2473	0.1696	0.0364	0.0545	0.0364
9	0.8893	0.6047	0.6245	0.4178	0.4222	0.4111	0.4580	0.5268	0.4643	0.5818	0.6000	0.7091

Table 6 Grey relational coefficient, grey relational grade, and their ranking

	Grey relational coefficient				Grey relational grade	
Exp. no	Aspect ratio	Microhardness	Surface roughness	Porosity	GRG	Rank
1 TR1	0.4210	0.6011	0.8550	0.9322	0.702299	4
1 TR2	0.4224	0.5880	0.7876	0.9322	0.682557	6
1 TR3	0.4196	0.5743	0.8485	0.9649	0.701825	5
2 TR1	0.4238	0.6731	0.9333	0.5238	0.638512	11
2 TR2	0.4238	0.6471	0.8034	0.5446	0.604721	14
2 TR3	0.4340	0.6386	0.9180	0.4622	0.613187	13
3 TR1	0.4478	1.0000	0.5209	0.6322	0.650225	9
3 TR2	0.4510	0.9004	0.5803	0.6180	0.637417	12
3 TR3	0.4462	0.7722	0.5147	0.5789	0.578018	16
4 TR1	0.3910	0.4619	0.4865	0.9322	0.567926	17
4 TR2	0.3898	0.4699	0.5545	0.9649	0.594763	15
4 TR3	0.3886	0.4511	0.4770	0.9322	0.562234	18
5 TR1	0.4462	0.4994	0.5528	0.6790	0.544347	19
5 TR2	0.4127	0.5105	0.4912	0.6790	0.523377	21
5 TR3	0.4154	0.5134	0.5545	0.6471	0.532598	20
6 TR1	0.9336	0.6875	0.9894	0.9649	0.893836	3
6 TR2	1.0000	0.7094	0.9349	1.0000	0.911071	1
6 TR3	0.9476	0.7228	1.0000	0.9649	0.908823	2
7 TR1	0.3351	0.3709	0.3963	0.3741	0.369117	25
7 TR2	0.3333	0.3813	0.3333	0.3333	0.345332	27
7 TR3	0.3910	0.3333	0.3684	0.3642	0.364257	26
8 TR1	0.4281	0.5484	0.7756	0.9322	0.671087	7
8 TR2	0.4310	0.5789	0.6691	0.9016	0.645142	10
8 TR3	0.4182	0.5805	0.7467	0.9322	0.669383	8
9 TR1	0.3599	0.5448	0.5219	0.4622	0.472192	24
9 TR2	0.4526	0.5422	0.4870	0.4545	0.484070	22
9 TR3	0.4446	0.5488	0.5185	0.4135	0.481364	23

Table 7 ANOVA results of the influence of process parameter

Parameter	Level 1	Level 2	Level 3	Deviation	Percentage	Rank
Laser power, W	0.5713	**0.5751**	0.4457	0.1293	26.33	2
Scanning speed, mm/min	0.4291	0.5013	**0.6617**	0.2326	47.36	1
Powder flow rate, g/min	**0.6118**	0.4825	0.4978	0.1293	26.31	3

The boldface was meant to distinguish the most significant values in Level 1, 2, and 3 respectively

using all the GRA experimental output as data and trained using the LMBP algorithm to predict GRG values. Thereafter, the mean square error (MSE) and the *R* value were used to measure the performance of the model computed using the transfer function utilizing the tangent sigmoid for hidden layers and output as a linear function model. This was based on the approach adopted by [15, 17, 30]. The hidden layer architecture was chosen because it gave the least MSE. The *R* values of 0.98883 training, 0.99968 testing, 0.99969 validating, and 0.99311 of the overall prediction were used to evaluate the performance of the model, as shown in Fig. 7. The trials using various network architectures are presented in Table 8. The network structure (3–4-1) gave the best value because of the lowest MSE, and the regression plot is shown in Fig. 7.

A random selection technique was used in choosing the data set for training, testing, and validation, with 80% of the data used for training, 10% for testing, and 10% for validation. The training focused on minimizing the MSE and the average prediction error (E_{tr}), computed by Eqs. 5 and 6, respectively. The best fit of the regression plot is presented in Fig. 7. Additionally, the ANN efficiency for predicting GRG values was explored by comparing the results with the average GRG output for experimental results, and the results are presented in Table 9. It can be seen that the ANN developed model has a better prediction

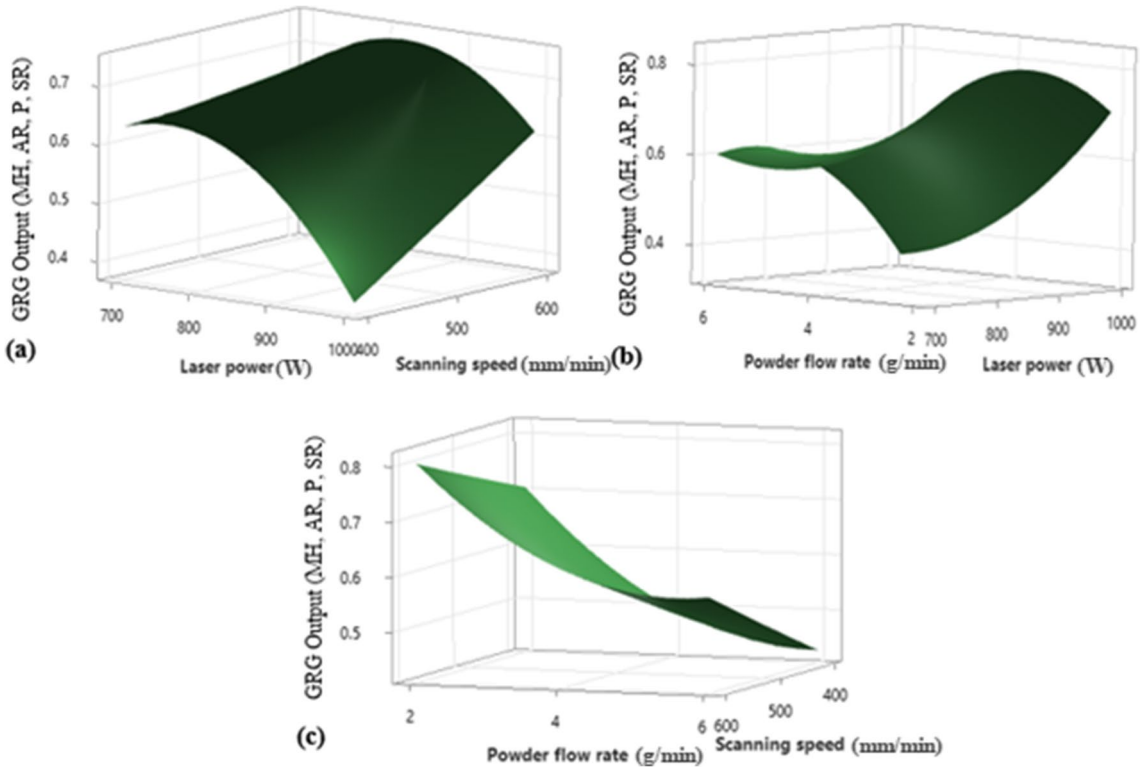

Fig. 5 Surface plot interaction of process parameters on GRG output for **a** scanning speed, laser power, **b** powder flow rate, laser power, and **c** powder flow rate, scanning speed

accuracy and the GRG obtained has a mean percentage error of 0.002 and a prediction accuracy of 99.15%, showing that the ANN model can be used for optimizing the experimental GRG (see Fig. 8).

$$MSE = \frac{1}{p}\sum_{p}\sum_{i}(T_{ip} - O_{ip})^2 \tag{5}$$

$$E_{tr}(y) = \frac{1}{N}\sum_{i=1}^{N}|(T_i(y) - O_i(y))| \tag{7}$$

Figure 8 establishes that the ANN predictive model agrees well with the experimental GRA, showing that the chosen architecture can be employed to predict the GRG of performance characteristics without carrying out

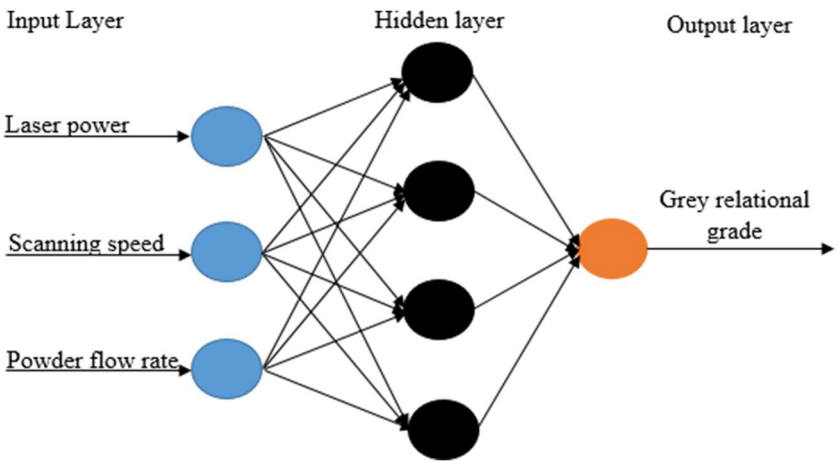

Fig. 6 Topology of the developed ANN model

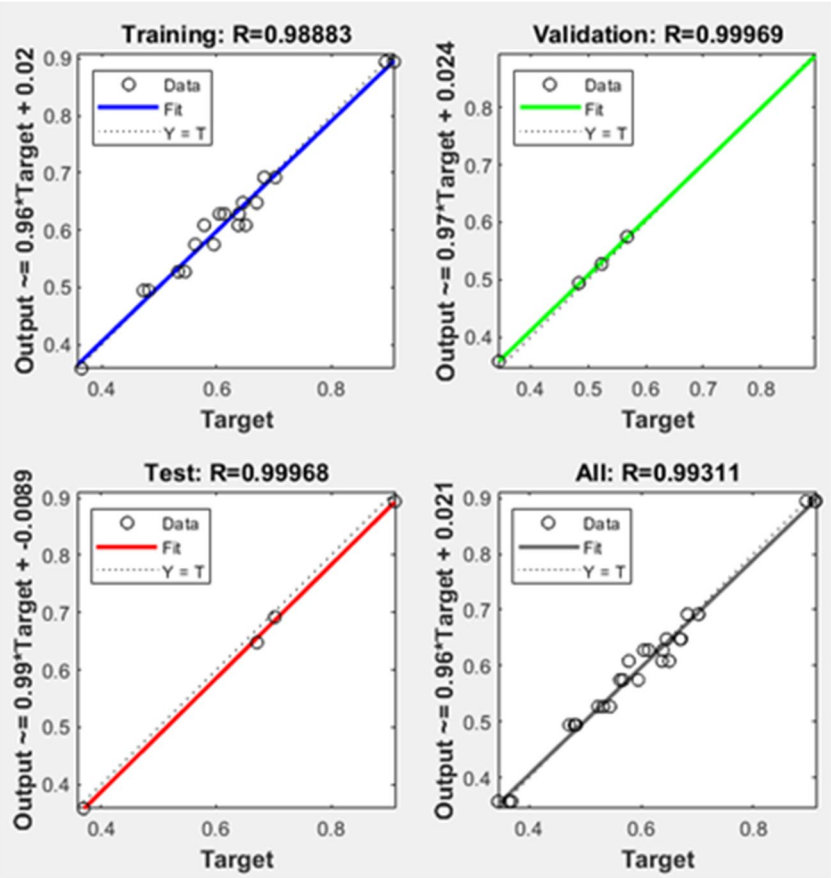

Fig. 7 Regression plot of the Levenberg–Marquardt back-propagation algorithm

experiments. It also affirms that the developed prediction model agrees well with the experimental results.

4 Effects of process parameter on clad quality characteristics

The fabricated samples were characterized and the influence of process parameters on the MH, AR, P, and SR attributes is detailed in this section.

4.1 Effects of process parameters on the microhardness properties

The main effects plots of laser power, scanning speed, and powder flow rate S/N ratios are shown in Fig. 9. It can be seen that microhardness increases when the scanning speed is increased from 400 to 600 mm/min (Fig. 9b). On the other hand, both laser power (Fig. 9a) and powder flow rate (Fig. 9c) have an inverse relationship with microhardness. This is affirmed by Table 10 that provides a summary of the

Table 8 Architecture for different trials employed in ANN predicting

Trial no	Network structure	Mean square error	*R* values			
			Training	Validation	Testing	All
1	3–2-1	0.0022	0.9012	0.9980	0.9987	0.9061
2	3–4-1	0.0001	0.9933	0.9970	0.9798	0.9889
3	3–6-1	0.0056	0.9882	1.0000	0.9940	0.9902
4	3–8-1	0.0002	0.9254	0.9988	0.9208	0.9419
5	3–10-1	0.0027	0.9968	0.9491	0.9836	0.9878
6	3–12-1	0.0038	0.9863	0.9905	0.9996	0.9901
7	3–14-1	4.0343e-04	0.9880	0.9996	0.9973	0.9901
8	3–16-1	4.2555e-04	0.9893	0.9999	0.9876	0.9901
9	3–18-1	0.0012	0.9684	0.9933	0.9995	0.9746
10	3–20-1	4.3435e-04	0.9899	0.9854	0.9534	0.9900

Table 9 Comparison of the GRG values predicted by ANN and those calculated by GRA

Trial no	Experimental GRG	ANN predicted GRG	Network error
1 TR1	0.702299	0.692045	0.010253
1 TR2	0.682557	0.628078	0.010433
1 TR3	0.701825	0.608563	0.041662
2 TR1	0.638512	0.574855	−0.006930
2 TR2	0.604721	0.527197	0.017150
2 TR3	0.613187	0.894094	−0.000259
3 TR1	0.650225	0.357876	0.011240
3 TR2	0.637417	0.647749	0.023337
3 TR3	0.578018	0.494340	−0.022148
4 TR1	0.567926	0.692045	−0.009488
4 TR2	0.594763	0.628078	−0.023357
4 TR3	0.562234	0.608563	0.028854
5 TR1	0.544347	0.574855	0.019908
5 TR2	0.523377	0.527197	−0.003820
5 TR3	0.532598	0.894094	0.016976
6 TR1	0.893836	0.357876	−0.012545
6 TR2	0.911071	0.647749	−0.002607
6 TR3	0.908823	0.494340	−0.010271
7 TR1	0.369117	0.692045	0.009780
7 TR2	0.345332	0.628078	−0.014891
7 TR3	0.364257	0.608563	−0.030545
8 TR1	0.671087	0.574855	−0.012622
8 TR2	0.645142	0.527197	0.0054008
8 TR3	0.669383	0.894094	0.0147286
9 TR1	0.472192	0.357876	0.0063804
9 TR2	0.484070	0.647749	0.021633
9 TR3	0.481364	0.494340	−0.012976

responses of the S/N ratios on microhardness. Based on the S/N responses, it can be deduced that the microhardness is most significantly influenced by scanning speed, followed by laser power and then powder flow rate.

This outcome can be attributed to the consolidation mechanism during LC process. According to Zhang et al. [35], adequate melting leads to grain refinement and microstructural enhancement responsible for promoting strong metallurgical bonds and higher microhardness. The FGM clad/substrate interface micrographs for the samples with the highest and lowest microhardness are shown in Fig. 10 for comparison. Figure 10a confirms that sample 6, which has the highest microhardness (HV), is characteristics by a dense microstructure without cracks, having a good consolidation with the substrate. This could be attributed to the laser-material interaction that decreases as the scanning speed is increased, leading to an adequate melting and enhanced microstructure with good metallurgical bonding without cracks. However, sample 7 that had the lowest microhardness (HV) was characterized by poor substrate bonding, interface cracks, and larger pores. The formation of defects is attributed to the higher laser power. When laser power is increased from 850 to 1000 W, the microhardness significantly reduced due to the high dilution and thermal stresses when the stress level exceeded the yield limit of the material. Additionally, when the powder flow rate increased from 4 to 6 g/min, the microhardness decreased. This is because excess powder requires more power and reduced scanning time for adequate melting. When these conditions are not met, there is insufficient bonding due to incomplete melting and pore and crack defect formation, as seen in Fig. 10b. Therefore, it can be inferred that poor consolidation and microstructural defects significantly reduced the FGM microhardness.

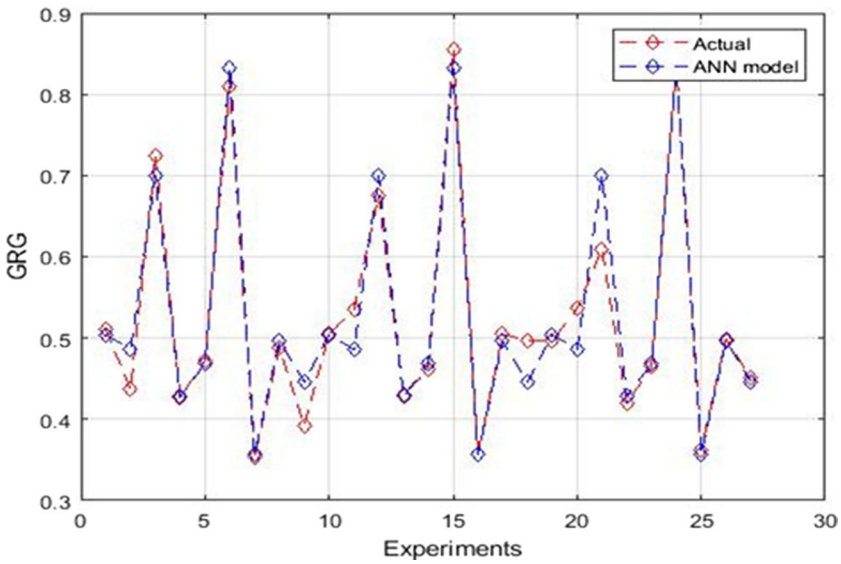

Fig. 8 Comparative analysis of ANN simulated GRG with the experimental GRG

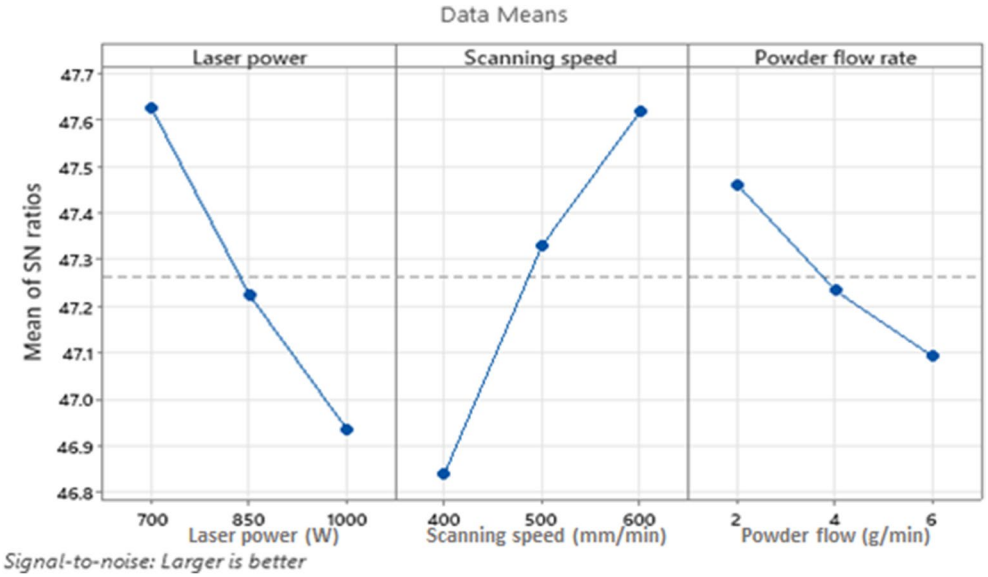

Fig. 9 Main effect plot for S/N ratios of the FGM microhardness

Table 10 Response table for the S/N ratios of the FGM microhardness. Larger is better

Level	Laser power	Scanning speed	Powder flow rate
1	47.62	46.84	47.46
2	47.22	47.33	47.23
3	46.94	47.62	47.09
Delta	0.69	0.78	0.37
Rank	2	1	3

Figure 11 shows the effects of process parameters interaction on microhardness. Figure 11a is developed by varying laser power and scanning speed, while powder flow rate was set at zero level value. The microhardness increased when the scanning speed was varied between 500-600 mm/min, with laser power set between 700-850 W. When the laser power is set to zero value, the microhardness is highest at powder flow rate of 2 g/min when scanning speed is set to the highest value of 600 mm/min, as shown in Fig. 11b. This

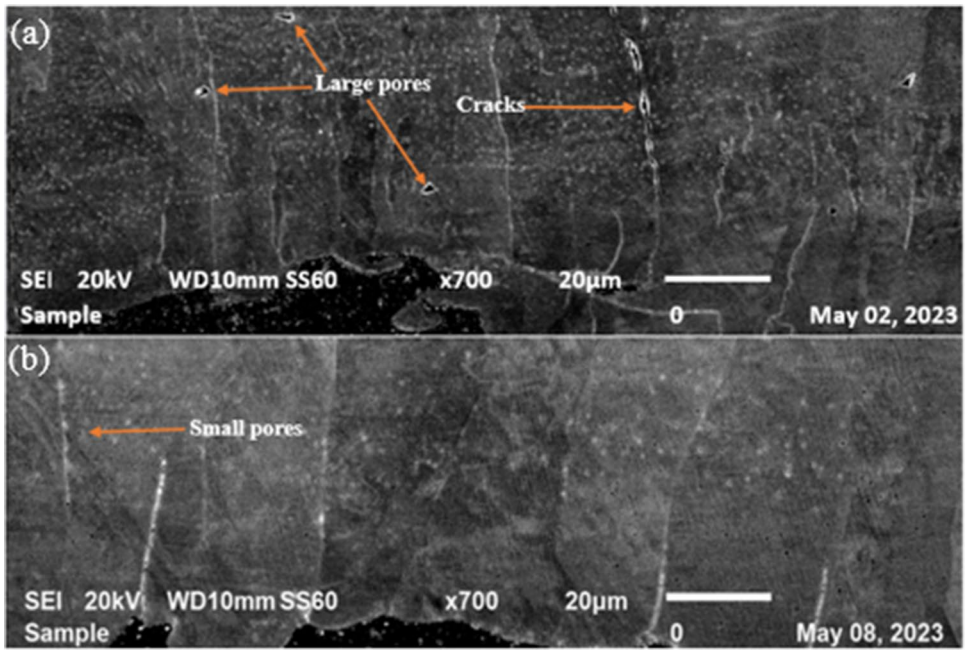

Fig. 10 SEM micrographs of FGM samples with **a** lowest microhardness for sample 7 and **b** highest microhardness for sample 6

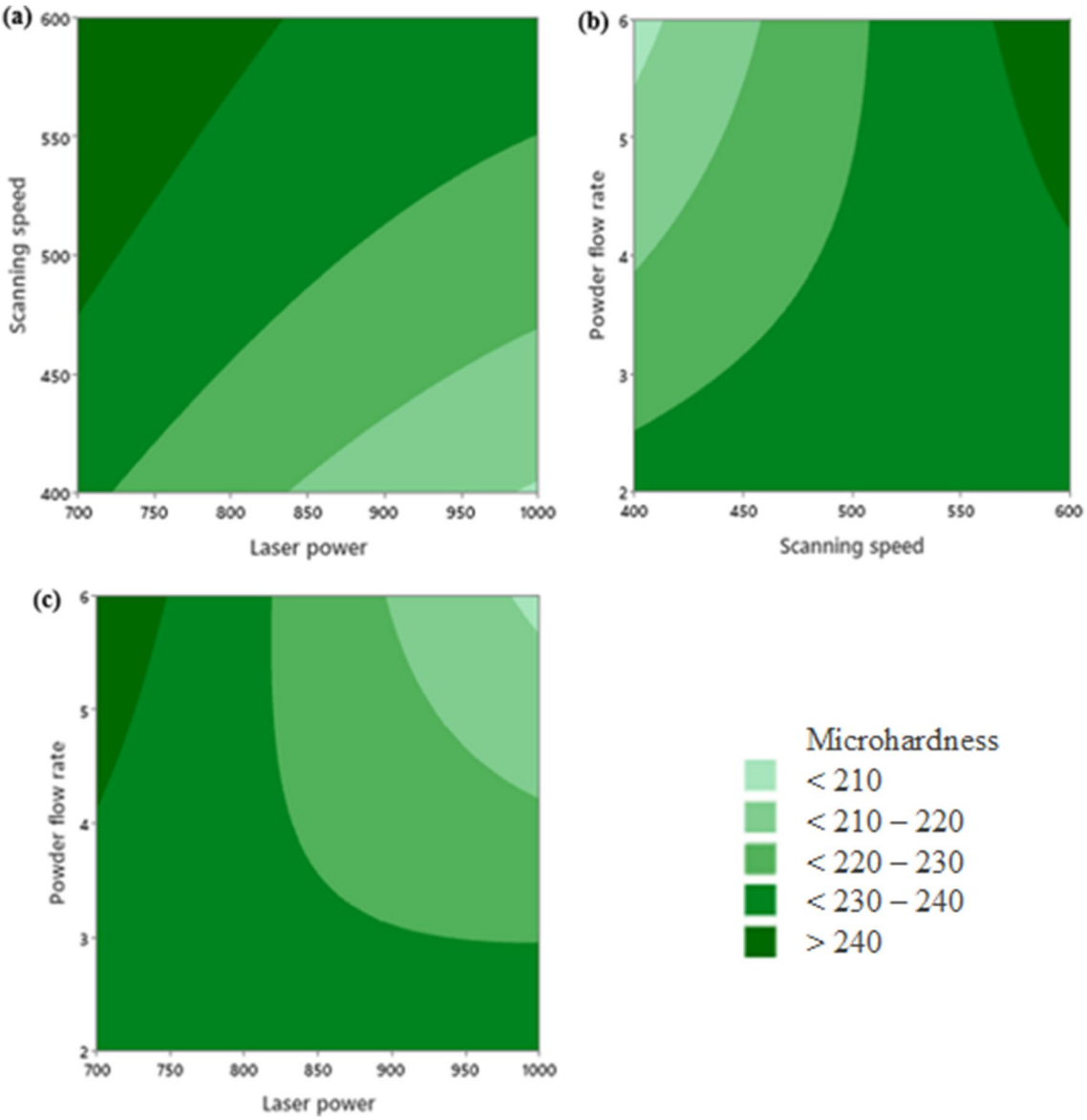

Fig. 11 Contour plots of the microhardness interaction effects of **a** laser power and scanning speed, **b** powder flow rate and scanning speed, and **c** laser power and powder flow rate

shows that increasing the powder rate and laser power to values greater than 4.5 g/min and 900 W, respectively, reduces the microhardness to less than 210 HV, as shown in Fig. 11c. Thus, it can be inferred that maximum hardness > 240 HV can be archived when scanning speed is higher than 6 mm/min, laser power between 700 and 850 W, and powder flow rate less than 2 g/min.

4.2 Effects of process parameters on AR

The main effect graphs of the process parameters on the AR are shown in Fig. 12. The results show that as scanning speed increases, the AR gets higher. When examining the effects of increasing speed on AR, Fatoba et al. [11] noticed the same correlation, which they attributed to the decrease in clad height that occurs when scanning speed is increased. They argued that scanning speed affects clad height in a greater way than clad width, which increases the AR in the process. AR increases when the molten pool increases as a result of widening clad width as the melt pool spreads. It is also clear from Fig. 12 that the AR increases to a certain threshold, then decreases gradually due to higher powder flow that leads to excessive clad buildup.

According to Table 11 for the S/N responses, the parameter that most significantly influences AR is scanning speed, followed by powder flow rate, and laser power has the least

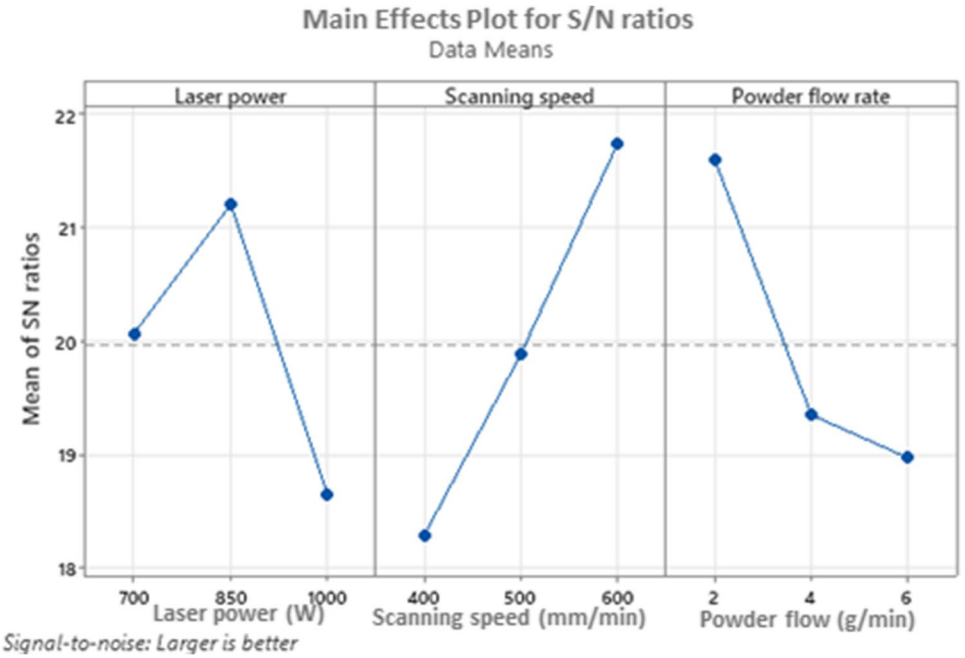

Fig. 12 Main effect plot for S/N ratios of the FGM aspect ratio

Table 11 Response table for the S/N ratios of the FGM microhardness

Level	Laser power	Scanning speed	Powder flow rate
1	20.06	18.29	21.60
2	21.20	19.88	19.35
3	18.65	21.74	18.97
Delta	2.55	3.45	2.63
Rank	3	1	2

Larger is better

significant impact. Generally, an increase in powder flow causes the clad height to increase, while reducing the clad height. This reduces the clad height and leads to a bulky layer coating.

In Fig. 13, contour plots are presented for AR interaction effects between laser power and scanning speed, powder flow rate and scanning speed, and powder flow rate and laser power. It is evident from Fig. 13 that AR is best maximized when the laser power is set at 750 to 900 W. However, when laser power is set outside the region of 950 to 1000 W, the AR reduces. Generally, increasing laser power increases the AR because it reduces clad height due to spreadibility of melt pool and widening of the clad height.

4.3 Effects of process parameter on porosity

Figure 14 shows the mean effect plot of smaller-the-better of the FGM porosity level. An increase in laser power from 700 to 1000 W and powder flow rate from 2 to 6 g/min increases the amount of porosity. Contrarywise, increasing scanning speed from 400 to 500 mm/min reduces the porosity level until it reaches a certain threshold, then it increases porosity at higher scanning speed reaching 6 mm/min.

A study of Fig. 15a,e,i indicates that the porosity increased as laser power increased from 700 to 1000 W. This can be explained by a larger molten pool attributed to higher heat input that results in gas entrapment and causes porosity according to Qi et al. [22]. Figure 15a and i shows that as powder flow rate increased from 2 to 6 g/min, the amount of porosity increased. This is because more energy input is used to melt more powder particles, resulting in some of the unmelted powder particles that lead to pore formation. It is also certain from Fig. 15c and d that an increase in scanning speed (400 to 500 mm/min) reduced the amount of porosity, but further increasing the scanning speed to 600 mm/min resulted in increased porosity, as shown in Fig. 15h. The porosity is attributed to unmelted particles because higher scanning speeds reaching 600 mm/min decrease the amount of energy input required for particle melting since it decreases the laser interaction time. Meanwhile, samples fabricated at lower scanning speeds of 400 mm/min lead to higher porosity level because it lowers the working temperature, which leads to partial melting, leaving some interparticle porosity. Therefore, it is evident that the amount of powder fed into the system and that melted significantly influence the porosity level. Table 12 ascertains that powder flow rate has the most influence on FGM porosity level, followed by laser power and scanning speed, respectively.

In Fig. 16, contour plots are used to illustrate the interactions between laser power and powder flow rate, powder

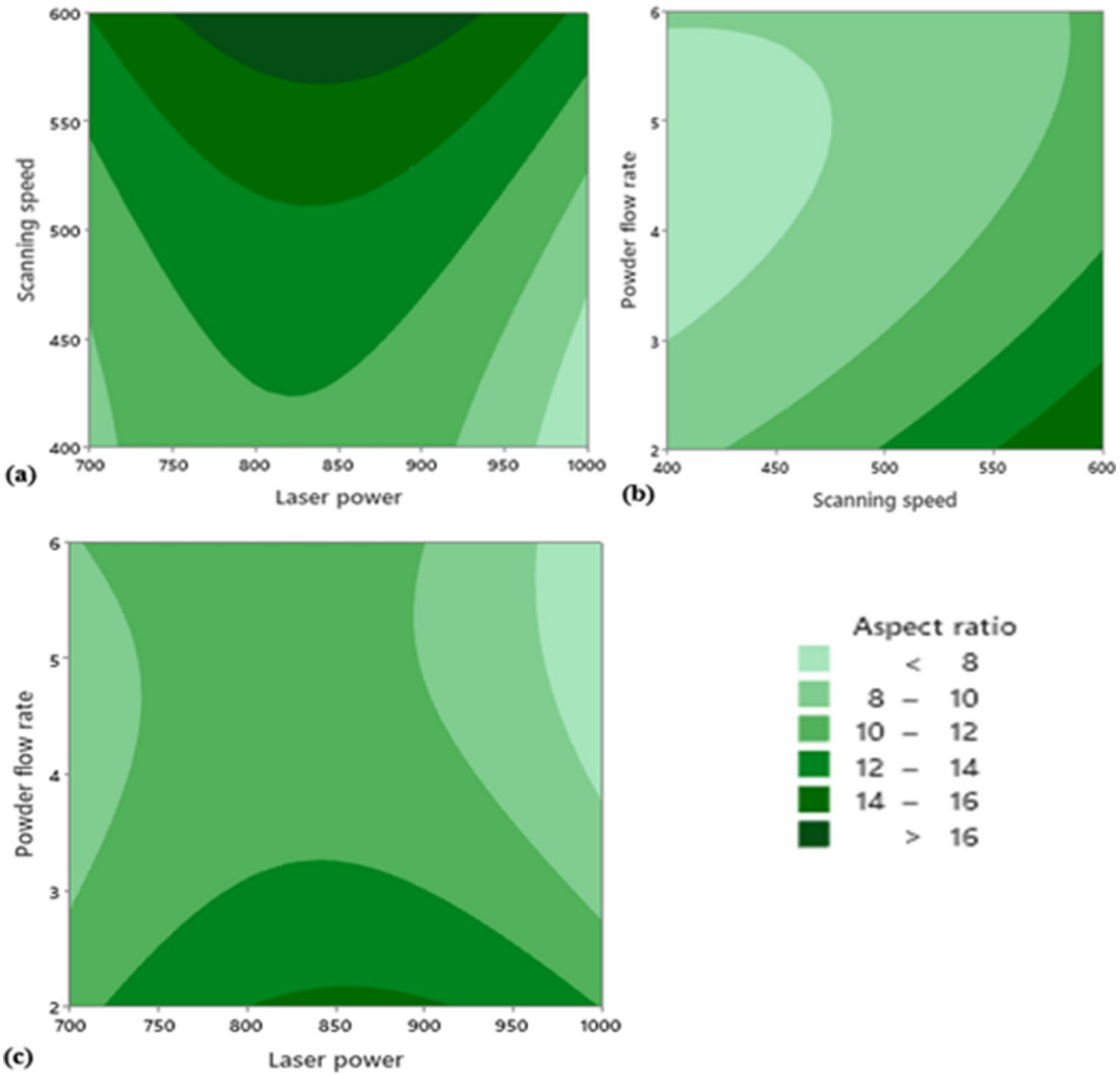

Fig. 13 Contour plots of the aspect ratio interaction effects of **a** scanning speed and laser power, **b** powder flow rate and scanning speed, and **c** powder flow rate and laser power

flow rate and scanning speed, and scanning speed and laser power on porosity. Two parameters were varied with the third kept at zero level. A porosity level > 0.3% is obtained when scanning speed is less than 450 mm/min and powder flow rate is more than 4 g/min. To obtain a porosity level less than 0.15%, the laser power must be set in the range between 750 and 850 W.

4.4 Effects of process parameter on surface roughness

Figure 17 shows the effect of process parameters on surface roughness. The surface roughness reduced as the laser power was increased up to a threshold of 850 W, then it increased with increasing laser power to 1000 W. Contrary, the surface roughness reduced with increase in scanning speed. Meanwhile, as the powder flow rate was increased, the surface roughness also increased. It can be seen from Table 13 that powder flow rate affects surface roughness the most, while laser power and scanning speed has the least influence, respectively. This is due to the fact that by raising the powder flow rate, insufficient particle melting occurs because the laser power was fixed, and the outcome is a rougher surface due to the unmelted particles according to Ahsan et al. [2]. Also, a lower laser power leads to unmelted powder particles that cause a higher surface roughness according to Mehrabi et al. [18].

Figure 18 indicates the interactive influence of two process parameters on the surface roughness while the other parameter is constant. The surface roughness would be

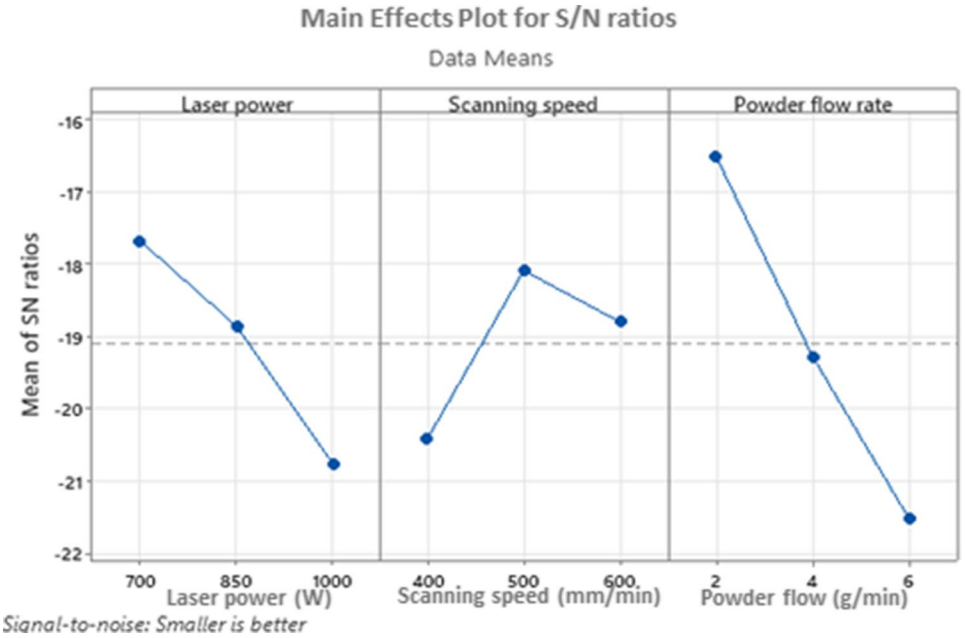

Fig. 14 Main effect plot for S/N ratios of the FGM porosity level

>14% when the scanning speed is <450 and laser power is between 950 and 1000 W (Figure 18a). When the powder flow rate is more than 5 g/min and the scanning speed is below 450 mm/min, the surface roughness would be >14% (Figure 18b). Meanwhile, a higher laser power > 950 W and higher powder flow rate >5 g/min would result in a higher surface roughness >14% (Figure 18c).

4.5 Confirmation and optimization

A one-factor-at-a-time confirmatory experiment was carried out using the well-trained network architecture as the simulating function. This was meant to determine the optimum process parameter that yields a higher GRA, because a higher GRA indicates the clad performance characteristics exhibit a higher microhardness and AR with reduced porosity and surface roughness. The model was simulated by varying one process parameter at a time while the two others remain constant. Figure 19a shows the optimization of laser power in the range of 300–1000 W, while scanning speed and powder flow rate were kept constant at 600 mm/s and 2 g/min, respectively. It can be seen that when laser power of 300–400 W is used, the GRA is at a minimum, which implies that it yields poor clad quality. Meanwhile, a higher GRA is obtained at a laser power of 600 W, which implies it is the optimum parameter that can improve the experimental LCs attributes. When the laser power is increased from 600 to 1000 W, the GRG values decrease significantly.

The ANN simulated model of laser power agrees with the experimental results because the optimum experimental laser power was 850 W when laser power was varied between 700 and 1000 W, with higher laser power producing poor claddings because of higher porosity attributed to the gas entrapment. Therefore, it is evident that the ANN GRG is higher than the GRG of the Taguchi-GRA method. Similarly, the GRG was improved when scanning speed was varied between 400 and 800 mm/min, as shown in Fig. 19b. The highest GRG values, which indicate the optimized scanning speed parameter, were found at 700 mm/min as compared to 600 mm/min from the LC experiment. Figure 13 also indicates that GRG is higher at 1.5 g/min when the powder flow rate is varied between 1 and 6 g/min, while laser power and scanning speed are kept constant at 700 W and 600 mm/min, respectively (see Fig. 19c). This shows that the GRG can be adjusted to optimize the clad quality characteristics, as it can be seen that GRG can be improved by ANN optimized parameters.

As such, a LC confirmatory experiment was carried out using the ANN optimized parameters, and the performance attributes of the GRA optimum sample were significantly improved compared to the initial Taguchi-GRA optimum sample (see Table 14). Results show that the ANN optimzed parameters enhance the clad quality characteristics of the microhardness, AR, porosity, and surface roughness by 5.8%, 5.4%, 50%, and 4.5%, respectively.

In subsequent paragraphs of this section, the nature of microstructural alteration, microhardness profile, dilution, and defects/residual stress analyses of the optimum sample is presented.

The microstructural evolution of the optimum sample is shown in Fig. 20. The five-layer clad morphologies of SS316L/IN625 FGM are shown in Fig. 20a. Due to the high weight percentage of SS316L, it can be seen that the first layers primarily consist of cellular and equiaxed structures

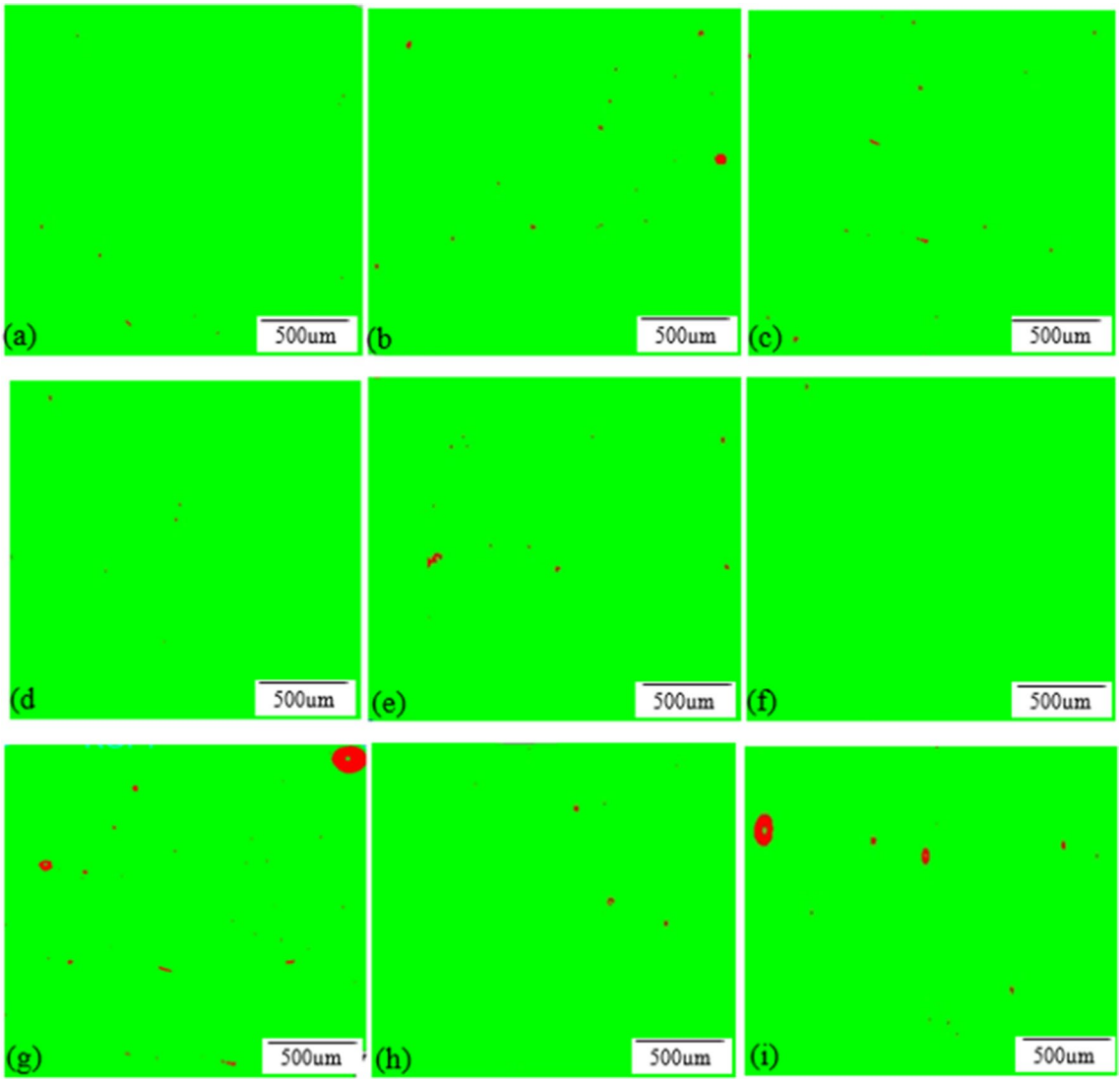

Fig. 15 Porosity analysis of FGM samples as a function of laser power: **a** 700 W, 0.04%; **e** 850 W, 0.15%; **i** 1000 W, 0.34%; **c** 400 mm/min, 0.18%; **d** 500 mm/min, 0.04%; **h** 600 mm/min, 0.05%; **f** 2 g/min, 0.03%; **b** 4 g/min, 0.27%; **g** 6 g/min, 0.48%

Table 12 Response table for the S/N ratios of the FGM porosity

Level	Laser power	Scanning speed	Powder flow rate
1	− 17.67	− 20.42	− 16.50
2	− 18.86	− 18.08	− 19.27
3	− 20.77	− 18.80	− 21.52
Delta	3.09	2.33	5.02
Rank	2	3	1

Smaller is better

expanding along the build direction, as shown in Fig. 20c and d.

However, the grain structure changes into the columnar dendritic structure as the layer builds up with the addition of IN625 to the matrix. This structure is mostly connected to IN625 and is triggered by a low-temperature gradient with rapid solidification according to Zhang et al. [32]. This shows that the variation in composition of the powders influenced the grain refinement and microstructural evolution of the FGM.

The Vickers hardness profile of Cu-SS316L-IN625 measured in the cross-sectional grading direction is shown in Fig. 21. The microhardness profile reveals that the Cu substrate had the lowest microhardness (119 ± 5 HV), which then significantly increased from SS316L (180 ± 0 HV) to the IN625 layer (245 ± 20 HV) that had the maximum microhardness. The hardness measurements found in the manufactured FGM are comparable to those mentioned by [18, 24]. The increased content of Laves phases and γ-dendrite in

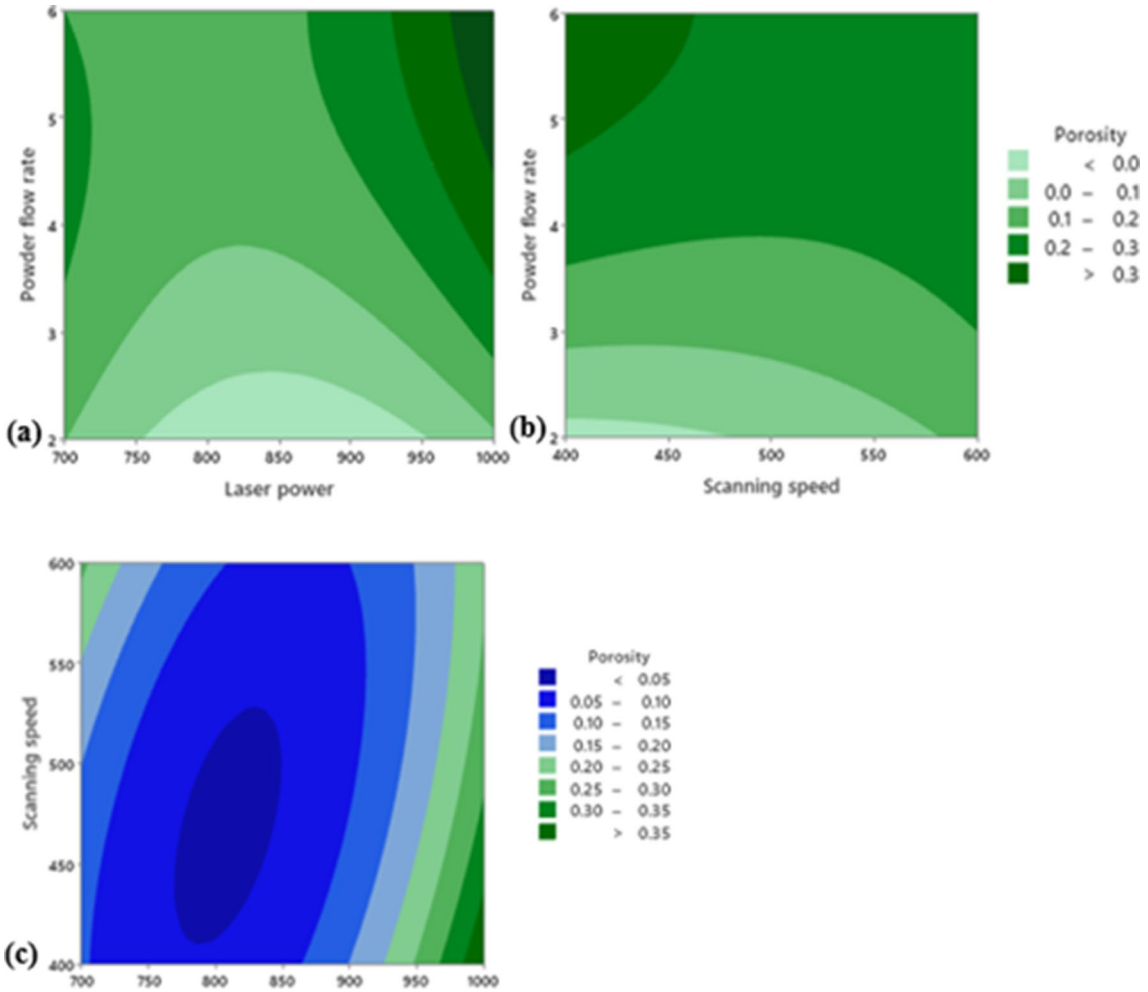

Fig. 16 Contour plots for the porosity interaction effects of **a** powder flow rate and laser power, **b** powder flow rate and scanning speed, and **c** scanning speed and laser power

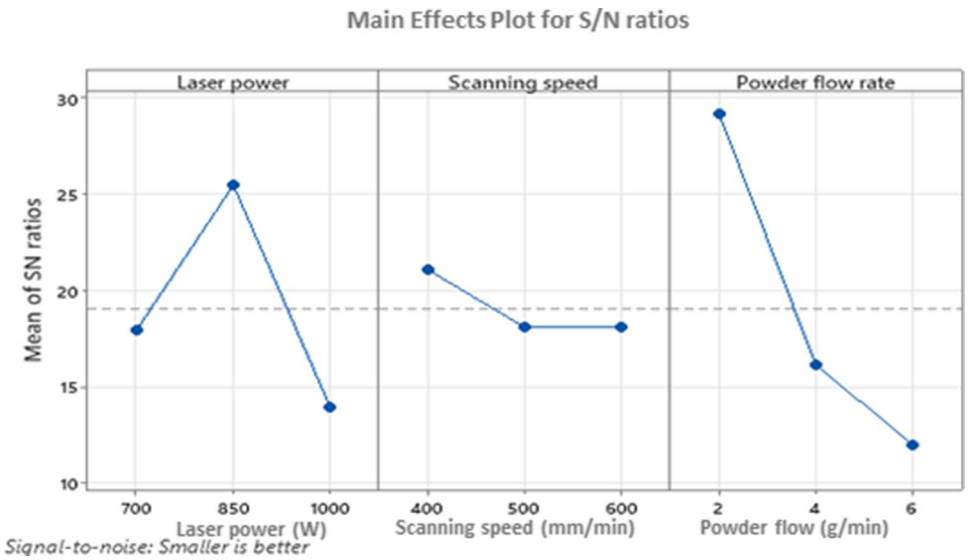

Fig. 17 Main effect plot for S/N ratios of the FGM surface roughness

Table 13 Response table for the S/N ratios of the FGM surface roughness

Level	Laser power	Scanning speed	Powder flow rate
1	17.90	21.05	29.15
2	25.43	18.07	16.09
3	13.90	18.11	11.99
Delta	11.53	2.98	17.17
Rank	2	3	1

Smaller is better

the interdendritic area promoted the solid solution strengthening of IN625, resulting in higher microhardness values (see Fig. 22). When functionally grading SS316L-IN625 using the LMD technique, Mehrabi et al. [18] observed the same matrix and linked the Laves phases and γ-matrix to the microhardness values.

Figure 23 shows the EDS analysis at the interface of the substrate and coating, which indicates the diffusion of chromium, iron, silicon, sulfur, and nickel elements to the copper substrate. This demonstrates that good metallurgical bonding with minimum dilution can be achieved when depositing at optimum processing parameters due to the adequate melting and diffusion of essential elements during laser-material interaction. The presence of Cr and Ni elements in the microstructure is preferred for better corrosion resistance of the copper substrate and FGM when operating in hostile conditions since they form a protective passive film. Minimum dilution is also preferred for coatings in order to enhance tribological properties and prevent customer rejection according to Maodzeka et al. [17].

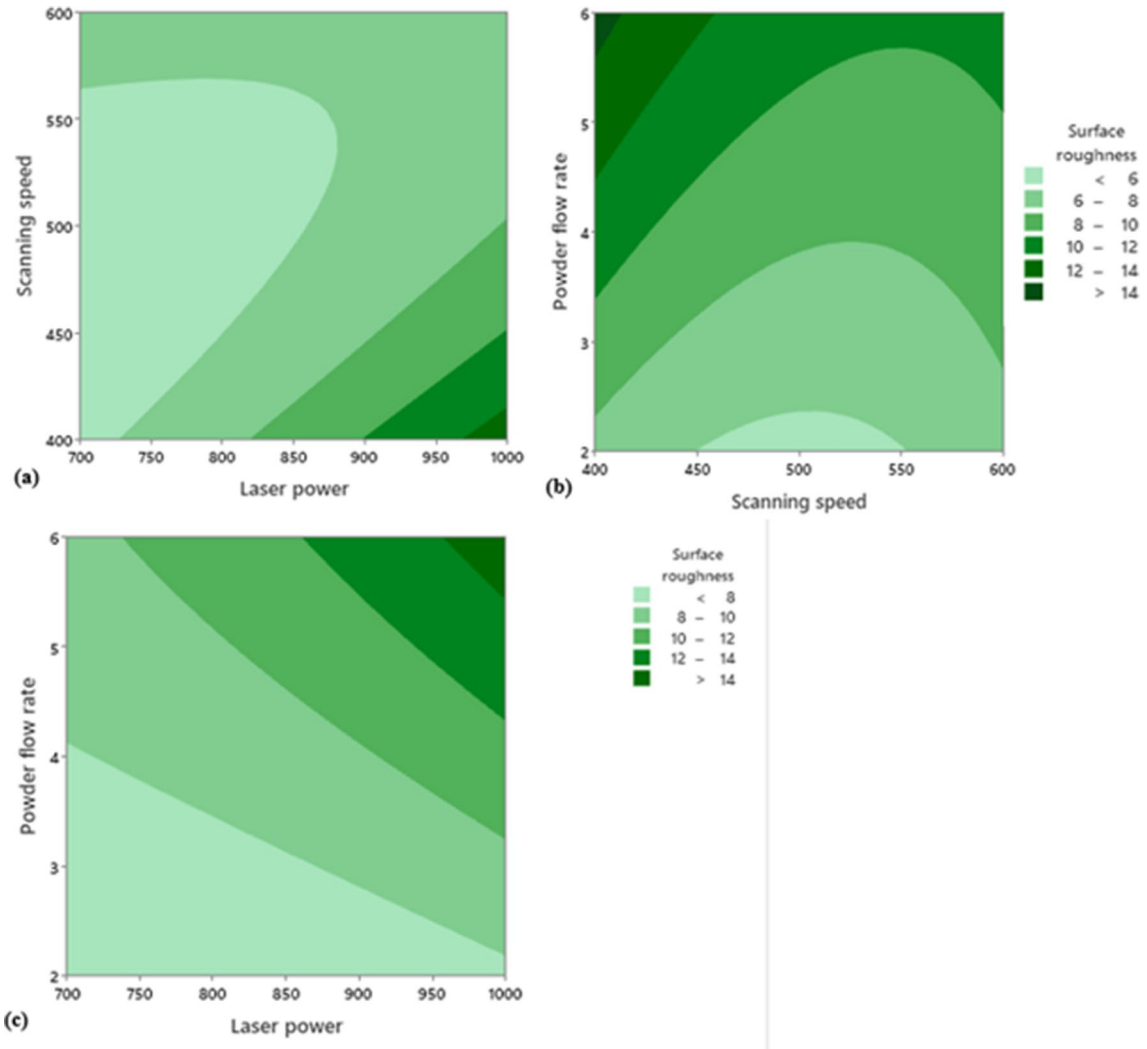

Fig. 18 Contour plots for the surface roughness interaction effects of **a** scanning speed and laser power, **b** powder flow rate and scanning speed, and **c** powder flow rate and laser power

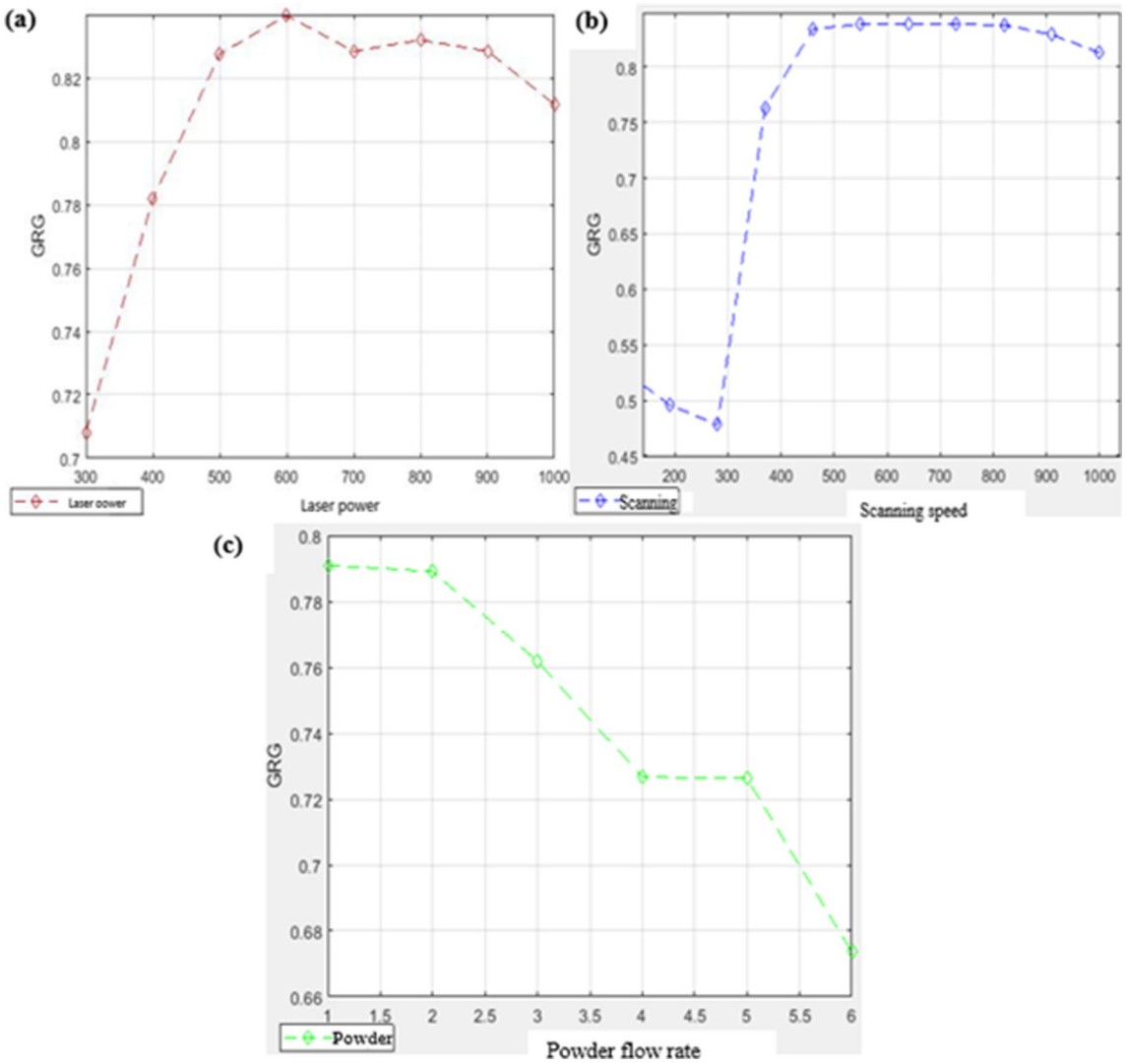

Fig. 19 Performance improvement of GRG values by varying **a** laser power, **b** scanning speed, and **c** powder flow rate

Table 14 Comparison between Taguchi optimum sample and ANN optimized sample

	Process parameter			Clad performance characteristics			
Sample	LP (W)	SP, mm/min	PF, g/min	MH, HV	AR, mm	PO, %	SR, Ra
Experimental Taguchi-GRA optimum	700	600	2.0	242.60	3.68	0.02	5.60
Predicted Taguchi-GRA	700	600	2.0	240.93	3.65	0.02	5.56
Experimental ANN optimized	600	700	1.5	257.41	3.89	0.01	5.35
Predicted ANN optimized	600	700	1.5	255.64	3.86	0.02	5.31

Tensile residual stresses that result in defects like pores and cracks that impair mechanical properties can be lessened with heat treatment post-processing. Figure 24 displays the residual stress readings for the heat-treated FGM, as-built coating, and pure copper substrate before deposition. The residual stress values were auto-generated by the residual stress machine. Figure 24a illustrates the findings, which demonstrate the stress distribution for pure copper that had compressive residual stresses of (− ve 2692 ± 300 MPa) that are acceptable for produced components. A homogeneous stress distribution can be seen by less distortion, an equilibrium debye ring, and a uniform stress profile on the substrate prior to deposition. The substrate and coating suffer expansion during the laser-material's interaction

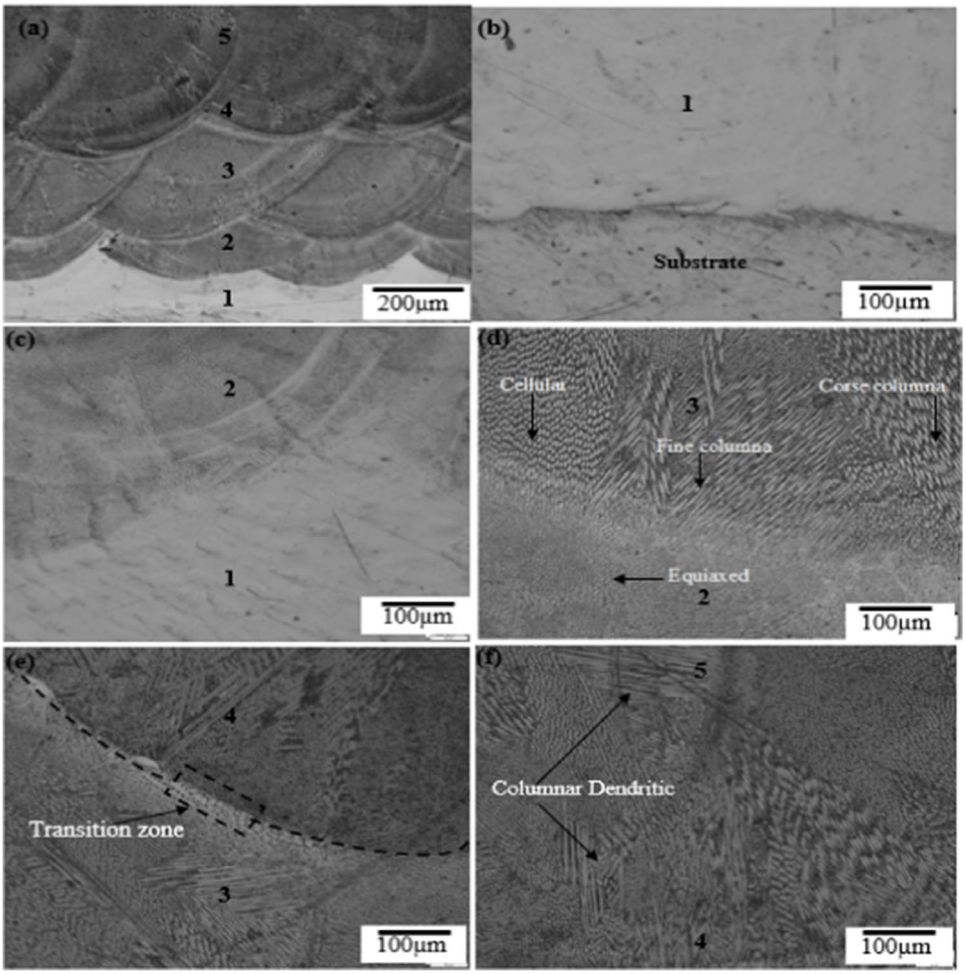

Fig. 20 Optical micrographs showing microstructural transformation of SS316L/IN625 FGM clad **a** microstructure of the clad geometry, **b** copper substrate/100%SS316L interface, **c** layers 1 and 2 interface, **d** layers 2 and 3 interface, **e** layers 3 and 4 interface, and **f** layers 4 and 5 interface

due to cooling and contraction, which results in tensile residual stresses (+ ve 8 ± 5 MPa) that distorts the material after LC according to Sadeh et al. [25]. This tensile RS can cause catastrophic failure of heat exchanger components through stress corrosion cracking due to high stress peaks highlighted in red, see Fig. 24b. The tensile residual stresses were reduced to compressive residual stresses after heat treatment (− ve 136 ± 15 MPa), as shown by the less distorted spectrum of Fig. 24c. It indicates that residual stresses lessen clad quality through defect formation, but process parameter optimization and heat treatment can improve the clad quality by lessening the tensile residual

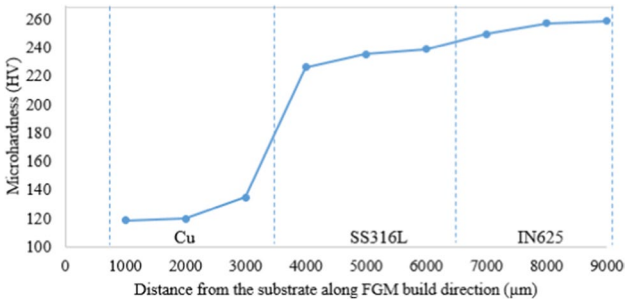

Fig. 21 Vickers microhardness profile of Cu substrate and SS316L/IN625 FGM along the clad build direction

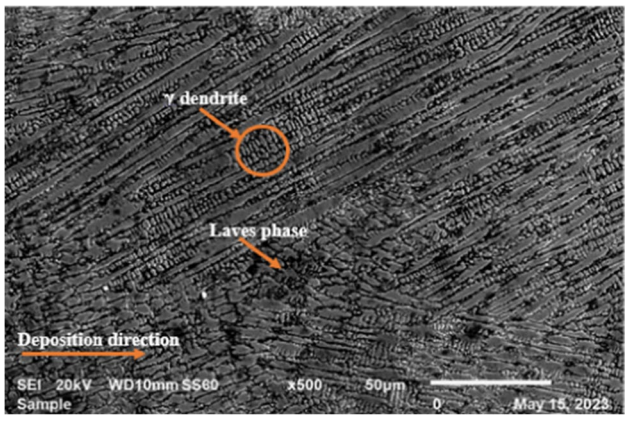

Fig. 22 SEM micrograph of the FGM microstructure at 50–50 wt.% of SS316L/IN625

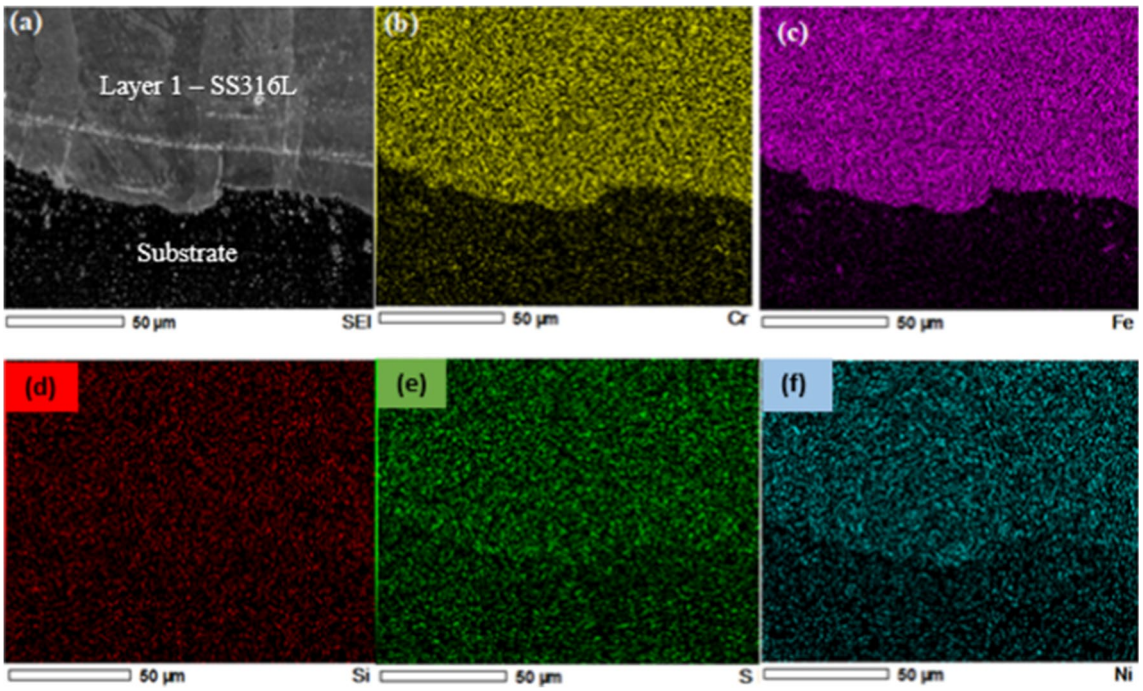

Fig. 23 The SEM–EDS mapping of the Cu-SS316L dilution zone **a** substrate/coating interface, and diffusion of **b** Cr, **c** Fe, **d** Si, **e** S, and **f** Ni

stresses in the manufactured FGM and identifying optimum conditions that reduce large thermal gradients.

5 Conclusions

In the present study, the hybrid Taguchi-GRA and ANN methods have been utilized as a solution to the multi-performance optimization of the LC process parameters. The effects of process parameters were correlated to the clad performance characteristics using microstructural analysis. The following conclusions were reached:

(a) Hybrid GRA-based TM has proven to be an effective technique and recommended for optimization of clad performance characteristics because of effective correlation of process parameters to output responses. Additionally, ANN optimized LC process parameters and produced quality FGM clads with high microhardness and AR, with no cracks and minimum porosity and surface roughness. This proved that it is a capable tool able to enhance performance characteristics by minimizing error function and by adjusting the weighted values of GRA output values.

(b) Scanning speed has the most significant influence on the SS316L/IN625 FGM clad performance characteristics, while powder flow rate and laser power have minimal effect.

(c) The optimal process parameters are laser power, scanning speed, and powder flow rate of 600 W, 700 mm/min, and 1.5 g/min, respectively. Under the optimum parameters, the clad quality characteristics were significantly improved.

(d) The SS36L/IN625 FGM comprises mostly of equiaxed structure that varied sharply to columnar grains as the layer buildup increased, due to rapid solidification and high thermal gradient attributed to the overlapping. The structure exhibited a good metallurgical bond between the substrate and coating due to sufficient powder melting, showing that the coating can be used for heat exchanger applications.

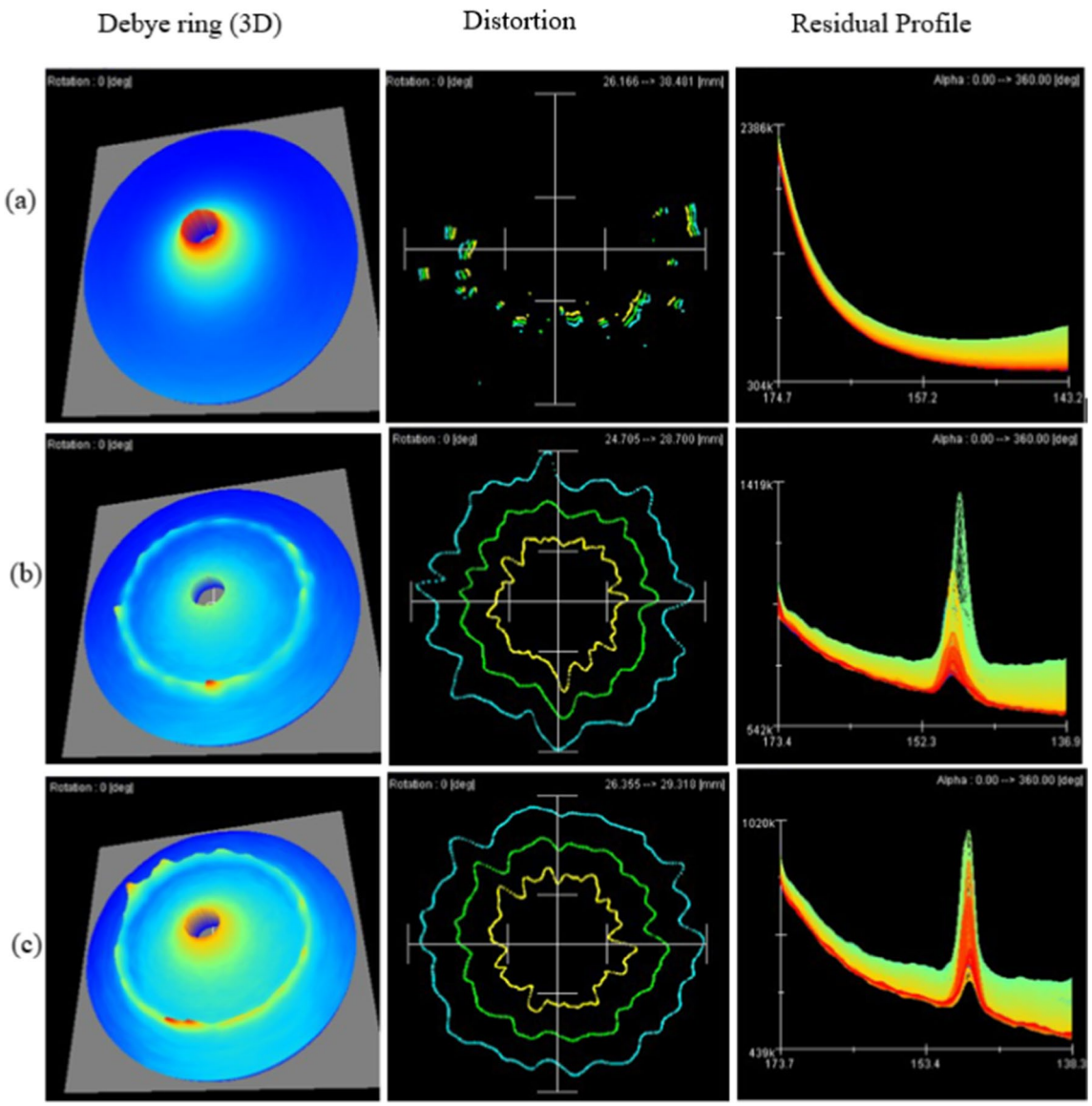

Fig. 24 Residual stress measurements of SS316L/IN625 FGM **a** pure copper substrate, **b** as-built SS316L/IN625 FGM, and **c** heat-treated cladding

Acknowledgements The authors would like to express their sincere gratitude to Mr Samuel Skhosane for assistance in operating the laser cladding machine at Council for Scientific and Industrial Research (CSIR), Pretoria.

Author contribution Conceptualization: JBM. Investigation: JBM, MRM, JMM, EOO, SLP. Methodology: JBM, MRM, JMM, EOO, SLP. Funding acquisition: JBM, EOO, SLP. Writing of the original draft: JBM. Writing of review and editing: JBM, MRM, JMM, EOO, SLP. All authors have read and agreed to the published version of the manuscript.

Funding This work was supported by the European Union, Fund No. 2019–1972/5, Project No. 61455. The African Laser Center also funded this work, Fund No. HLHA24X task ALC-R020. Mr Joseph Morake, who is the first author, is the first author to receive the funding.

European Commission,2019-1973/5,Joseph Bophelo Morake,614655,Joseph Bophelo Morake

Data availability All the data used is available within the manuscript. Any additional simulation information can be obtained from the first author upon request.

Declarations

Competing interests The authors declare no competing interests.

References

1. Abioye TE, McCartney DG, Clare AT (2015) Laser cladding of Inconel 625 wire for corrosion protection. J Mater Process Technol 217:232–240. https://doi.org/10.1016/j.jmatprotec.2014.10.024
2. Ahsan MN, Pinkerton AJ, Moat RJ, Shackleton J (2011) A comparative study of laser direct metal deposition characteristics using gas and plasma-atomized Ti-6Al-4V powders. Mater Sci Eng, A 528(25–26):7648–7657. https://doi.org/10.1016/j.msea.2011.06.074
3. Alam MK, Urbanic RJ, Nazemi N, Edrisy A (2018) Predictive modeling and the effect of process parameters on the hardness and bead characteristics for laser-cladded stainless steel. Int J Adv Manuf Technol 94(1–4):397–413. https://doi.org/10.1007/s00170-017-0898-5
4. Ali M, Ul-Hamid A, Alhems LM, Saeed A (2020) Review of common failures in heat exchangers – part I: mechanical and elevated temperature failures. Eng Fail Anal 109:104396. https://doi.org/10.1016/j.engfailanal.2020.104396
5. Carroll BE, Otis RA, Borgonia JP, Suh JO, Dillon RP, Shapiro AA, Hofmann DC, Liu ZK, Beese AM (2016) Functionally graded material of 304L stainless steel and inconel 625 fabricated by directed energy deposition: characterization and thermodynamic modeling. Acta Mater 108:46–54. https://doi.org/10.1016/j.actamat.2016.02.019
6. Chae H, Wang H, Hong M, Kim WC, Kim JG, Kim H, Lee SY (2020) Stress corrosion cracking of a copper pipe in a heating water supply system. Met Mater Int 26(7):989–997. https://doi.org/10.1007/s12540-019-00386-0
7. Chang YY, Qiu JR, Hwang SJ (2022) Multi-objective optimization of directed energy deposition process by using Taguchi-Grey relational analysis. Int J Adv Manuf Technol 120(11–12):7547–7563. https://doi.org/10.1007/s00170-022-09210-3
8. Cozzarini L, Marsich L, Schmid C (2020) Ant-nest corrosion failure of heat exchangers copper pipes. Eng Fail Anal 109:104387. https://doi.org/10.1016/j.engfailanal.2020.104387
9. Elijah K-A (2009) Materials processing principles of laser. In: Source. John Wiley & Sons, Inc., Hoboken, New Jersey
10. Faes W, Lecompte S, Ahmed ZY, Van Bael J, Salenbien R, Verbeken K, De Paepe M (2019) Corrosion and corrosion prevention in heat exchangers. Corros Rev 37(2):131–155. https://doi.org/10.1515/corrrev-2018-0054
11. Fatoba OS, Naidoo L, Akinlabi SA, Akinlabi ET, Mwema FM, Ikumapayi OM (2021) Dilution and aspect ratio properties on performance of laser deposited Ti-Al-Si-Cu/Ti-6Al-4V composite coatings. IOP Conf Series: Mater Sci Eng 1107(1):012123. https://doi.org/10.1088/1757-899x/1107/1/012123
12. Koklu U, Mayday M, Morkavuk S, Aver A, Demir O (2019) Optimization and prediction of thrust force, vibration and delamination in drilling of functionally graded composite using Taguchi, ANOVA and ANN analysis. Mater Res Express (6). https://doi.org/10.1088/2053-1591/ab2617
13. Kuźnicka B (2009) Erosion-corrosion of heat exchanger tubes. Eng Fail Anal 16(7):2382–2387. https://doi.org/10.1016/j.engfailanal.2009.03.026
14. Liang X, Wu D, Li Q, Jiang L (2010) Laser rapid manufacturing of stainless steel 316L/Inconel718 functionally graded materials: microstructure evolution and mechanical properties. Int J Optics 2010:1–6. https://doi.org/10.1155/2010/802385
15. Lin HL (2012) The use of the Taguchi method with grey relational analysis and a neural network to optimize a novel GMA welding process. J Intell Manuf 23(5):1671–1680. https://doi.org/10.1007/s10845-010-0468-2
16. Manikandan N, Palanisamy D (2020) Optimisation of spark erosion machining process parameters using hybrid grey relational analysis and artificial neural network model Ramesh Raju 22(1). https://doi.org/10.1504/IJMMM.2020.104007
17. Maodzeka DK, Olakanmi EO, Mosalagae M, Hagedorn-Hansen D, Pityana SL (2023) Hybrid optimisation studies on the microstructural properties and wear resistance of maraging steel 1.2709 parts produced by laser powder bed fusion. Optics Laser Technol 159:108914. https://doi.org/10.1016/j.optlastec.2022.108914
18. Mehrabi O, Mohammad S, Seyedkashi H (2023) Functionally graded additive manufacturing of thin-walled 316L stainless steel-Inconel 625 by direct laser metal deposition process: characterization and evaluation. https://doi.org/10.3390/met13061108
19. Ndumia JN, Kang M, Gbenontin BV, Lin J, Nyambura SM (2021) A review on the wear, corrosion and high-temperature resistant properties of wire arc-sprayed fe-based coatings. Nanomaterials, 11(10). https://doi.org/10.3390/nano11102527
20. Olakanmi EO, Nyadongo ST, Malikongwa K, Lawal SA, Botes A, Pityana SL (2019) Multi-variable optimisation of the quality characteristics of fiber-laser cladded Inconel-625 composite coatings. Surf Coatings Technol 357:289–303. https://doi.org/10.1016/j.surfcoat.2018.09.063
21. Owoputi AO, Inambao FL, Ebhota WS (2018) A review of functionally graded materials: fabrication processes and applications. Int J Appl Eng Res 13(23):16141–16151
22. Qi H, Azer M, Ritter A (2009) Studies of standard heat treatment effects on microstructure and mechanical properties of laser net shape manufactured Inconel 718. Metall Mater Trans A 40(10):2410–2422. https://doi.org/10.1007/s11661-009-9949-3
23. Riveiro A, Mejías A, Lusquiños F, Del Val J, Comesaña R, Pardo J, Pou J (2013) Optimization of laser cladding for Al coating production. Phys Procedia 41:327–334. https://doi.org/10.1016/j.phpro.2013.03.085
24. Rodrigues TA, Cipriano Farias FW, Zhang K, Shamsolhodaei A, Shen J, Zhou N, Schell N, Capek J, Polatidis E, Santos TG, Oliveira JP (2022) Wire and arc additive manufacturing of 316L stainless steel/Inconel 625 functionally graded material: development and characterization. J Market Res 21:237–251. https://doi.org/10.1016/j.jmrt.2022.08.169
25. Sadeh S, Mathews R, Zhang R, Sunny S, Marais D, Venter AM, Li W, Malik A (2023) Interlayer machining effects on microstructure and residual stress in directed energy deposition of stainless steel 316L. J Manuf Process 94:69–78. https://doi.org/10.1016/j.jmapro.2023.03.036
26. Simeon O, Stephen O, Akinlabi A, Madushele N, Samuel O, Akinlabi ET (2023) Multi-response optimization of TIG dissimilar welding of AISI 1008 mild steel and AISI 316 stainless steel using grey-based Taguchi method. Int J AdvManuf Technol. 0123456789.https://doi.org/10.1007/s00170-023-11080-2
27. Soltani A, Najafi M, Ghorbani R, Danaei R (2016) Failure analysis of cracks occurred on SS304L tubes of shell and tube heat exchanger during its first start up in phases 2&3 gas refinery of South Pars gas complex. Eur Corros Congress, EUROCORR 2016(4):3090–3100

28. Tiwari GK, Dubey AK, Siddiqui AA (2020) A hybrid approach for modelling and optimization of laser cladding process. Int J Adv Prod Ind Eng 5(1):17–24. https://doi.org/10.35121/ijapie202001142
29. Vikram Reddy V, Vamshi Krishna P, Jawahar M, Shiva Kumar B (2018) Optimization of process parameters during EDM of SS304 using Taguchi-grey relational analysis. Mater Today: Proc 5(13):27065–27071. https://doi.org/10.1016/j.matpr.2018.09.011
30. Wakchaure KN, Thakur AG, Gadakh V, Kumar A (2018) Multi-objective optimization of friction stir welding of aluminium alloy 6082–T6 using hybrid Taguchi-grey relation analysis-ANN method. Mater Today: Proc 5(2):7150–7159. https://doi.org/10.1016/j.matpr.2017.11.380
31. Yang B, Lai Y, Yue X, Wang D, Zhao Y (2020) Parametric optimization of laser additive manufacturing of Inconel 625 using Taguchi method and grey relational analysis. Scanning, 2020. https://doi.org/10.1155/2020/9176509
32. Zhang X, Chen Y, Liou F (2019) Fabrication of SS316L-IN625 functionally graded materials by powder-fed directed energy deposition. Sci Technol Weld Join 0(0):1–13. https://doi.org/10.1080/13621718.2019.1589086
33. Zhang X, Chen Y, Liou F (2019b). Fabrication of SS316L-IN625 functionally graded materials by powder-fed fabrication of SS316L-IN625 functionally graded materials by powder-fed directed energy deposition. October 2020. https://doi.org/10.1080/13621718.2019.1589086
34. Zhang, X., Pan, T., Flood, A., Chen, Y., Zhang, Y., & Liou, F. (2021). Investigation of copper/stainless steel multi-metallic materials fabricated by laser metal deposition.Mater Sci Eng A, 811. https://doi.org/10.1016/j.msea.2021.141071
35. Zhang YZ, Tu Y, Xi MZ, Shi LK (2008) Characterization on laser clad nickel based alloy coating on pure copper. Surf Coatings Technol 202(24):5924–5928. https://doi.org/10.1016/j.surfcoat.2008.06.163
36. Morake JB, Mutua JM, Maina RM, Olakanmi EO (2023) The potential use of laser cladded functionally graded materials to mitigate degradation in boiler tube heat exchangers for power plant applications: a review. Surf Eng 39(6):677–721. https://doi.org/10.1080/02670844.2023.2249653